Worrying drives cell migration in mechanically unrestrained environments

Erik S. Welf,[1,2,*] Meghan K. Driscoll,[1,2,*] Etai Sapoznik,[2] Vasanth S. Murali,[1,2] Andrew Weems,[1,2] Minna Roh-Johnson,[3] Kevin M. Dean,[2] Reto Fiolka,[2,§] Gaudenz Danuser[1,2,§]

[1]Department of Bioinformatics, University of Texas Southwestern Medical Center, Dallas, TX
[2]Department of Cell Biology, University of Texas Southwestern Medical Center, Dallas, TX
[3]Department of Biochemistry, School of Medicine, University of Utah, Salt Lake City, UT
*Contributed equally,
[§]Corresponding author, Gaudenz.Danuser@UTSouthwestern.edu, Reto.Fiolka@UTSouthwestern.edu

Abstract

Migratory cells employ numerous strategies to navigate the very diverse 3D microenvironments found *in vivo*. These strategies are subdivided into those that create space by pericellular proteolysis of extracellular matrix (ECM) proteins and those that navigate existing spaces. We find that cells can employ an alternative mechanism by digging tunnels through 3D collagen networks without extracellular proteolysis. This is accomplished by persistent polarization of large dynamic membrane blebs at the closed end of the tunnel that repeatedly agitate the collagen, a process we termed mechanical worrying. We find that this agitation promotes breakage and internalization of collagen at the cell front along with extracellular fluid in a macropinocytosis-driven manner. Membrane blebs are short-lived relative to the timescale of migration, and thus their polarization is critical for persistent ablation of the ECM. We find that sustained interactions between the collagen at the cell front and small but persistent cortical adhesions induce PI-3 Kinase (PI3K) signaling that drives polarized bleb enlargement via the Rac1 – Arp2/3 pathway. This defines a mechanism for the reinforcement of bleb expansion against load, which enables precise ablation of mechanically unrestrained environments, such as those encountered in very compliant tissue.

Introduction

Cell movement through dense 3D microenvironments is a fundamental requirement for a wide variety of biological processes, including tissue development and homeostasis, immune surveillance, and also metastatic dissemination. To accomplish this, cells adopt different motility modes depending on their lineage and the properties of the microenvironment. Tissues are composites made up of both soft and stiff materials (Bonnans et al., 2014; Handorf et al., 2015) and so cell migration strategies must be able to account for a range of stiffnesses. The most studied form of migration involves a pulling mechanism whereby cells crawl across a flat, stiff plane by adhering strongly at the front and contracting to pull themselves along (Abercrombie et al., 1970; Lauffenburger and Horwitz, 1996). Other cell types migrate by exerting strong pushing forces at their rear (Jannat et al., 2011). The common requirement for these migration modes is a surface that resists forces placed on them by the cell. Yet such flat, stiff surfaces likely represent only a small fraction of *in vivo* microenvironments. Likewise, the most commonly studied 3D migration modes also require stiff or restrained microenvironments in order to resist pulling or pushing forces (Yamada and Sixt, 2019). Even cells that generate protrusion by recently discovered mechanisms of cytoplasmic force generation require compression of the cell's nucleus by the microenvironment (Petrie et al., 2014; Stroka et al., 2014). Indeed, the nucleus has emerged as a critical regulator of 3D cell migration (Calero-Cuenca et al., 2018; Petrie and Yamada, 2016). The relatively large and incompressible nucleus restricts migration through small openings and thus movement through tortuous environments requires

the ability to either sense pore size and find routes with larger pores (Lomakin et al., 2020; Renkawitz et al., 2019) or deform the nucleus to squeeze through existing pores (Denais et al., 2016). Compression of the nucleus itself can even modulate cell migration mode (Venturini et al., 2020). A common theme in all these studies is the interaction of cells with materials that are sufficiently stiff to resist pushing or pulling or cause deformation of the nucleus. Because these 3D motility mechanisms require confinement and mechanical resistance from the microenvironment in order to balance the forces exerted by cells, it raises the question of what mechanisms cells use to move through compliant microenvironments, such as those found, for example, in the dermal stroma or brain, which are mechanically much less restrained than typical synthetic microenvironments and even less stiff than a cell nucleus (Guimarães et al., 2020; Lammerding, 2011).

Experimental challenges complicate the study of cell migration in highly compliant environments. First, round cells are commonly observed in soft microenvironments (Boekhorst et al., 2020; Georgouli et al., 2019; Sahai and Marshall, 2003), yet due to their lack of obvious morphological polarity may have been assumed to be immobile. Second, almost all high resolution microscopes capable of capturing molecular activity require close proximity of cells and the ECM to glass and/or other hard surfaces; and even low resolution imaging of cell motility is often performed near a coverslip (Wolf et al., 2013). Adsorption of collagen to these stiff surfaces means that, despite soft bulk material properties, deformation is restrained (Ma and Baumgartner, 2013; Provenzano et al., 2009; Rao et al., 2012; Wang et al., 2014), and cells perceive these ECM conditions as stiff (Welf et al., 2016).

To overcome the technical barriers of examining migration in mechanically unrestrained environments, we previously developed specialized light-sheet microscopes and sample chambers that permit high resolution imaging of cells in microenvironments roughly 1 mm away from the microscope lens and any other stiff surface, effectively eliminating mechanical influences on cell behavior from any material besides the ECM network (Dean et al., 2015; Welf et al., 2016). Under these conditions, we found that cancer cells exhibit a slow but directed motion resulting from the persistent and methodical application of pressure-based membrane blebs that mechanically wear away the malleable ECM. We refer to this mode as mechanical worrying, following the definition of worrying given by the Mirriam Webster Dictionary as “to harass by tearing, biting, or snapping”. This worrying action produces a tunnel that serves as a forensic record of cell motility over long periods of time. Surprisingly, this process does not require extracellular proteases, but instead utilizes directed cellular internalization to remove mechanically agitated, worn-out collagen from the tunnel front, enabling destructive cell invasion without enzymatic cleavage. Furthermore, we find that mechanical worrying uses similar molecular pathways as other migration modes, namely polarized adhesions, phosphoinositide-3 kinase, Rac1, and actin polymerization. In contrast to other well-described bleb-based migration modes (Paluch and Raz, 2013), worrying functions by concentrating these factors at the front of a tunneling cell to enlarge membrane blebs, suggesting that the level of bleb expansion necessary for productive worrying requires actin polymerization in addition to intracellular pressure. Thus, the worrying migration mode, in a unique fashion, exploits the full repertoire of protrusion force generation tools to generate a path under mechanically challenging conditions.

Results

To study cell migration in mechanically unrestrained microenvironments, we created *in vivo* mimetics by using specially designed sample chambers to encapsulate cells in 3D gels formed by Collagen I polymer networks. This resulted in microenvironments with stiffnesses on the order of 1 kPa (Bordeleau et al.,

2017; Burla et al., 2020). The chambers enable imaging with our meSPIM and ASLM light-sheet microscopes, both of which exhibit near-isotropic spatial resolution of approximately 300 nm (Dean et al., 2015; Welf et al., 2016), which enables spatially unbiased 3D computational analysis of the morphology and membrane-associated signals (Driscoll et al., 2019). Although purified collagen does not completely recapitulate the complexities of the *in vivo* microenvironment, it is the most abundant ECM protein in the body, and when polymerized creates a dense gel that offers an alternative to the rigid and mechanically constrained environments most often used to study 3D cell migration (Sherman et al., 2015).

As a prototypal cell model, we used metastatic melanoma, for which movement through soft environments is a hallmark of metastatic disease. For example, the first phase of metastatic dissemination in melanoma is the transition from a radial growth phase to a vertical growth phase, whereby cells invade the largely acellular and relatively soft dermal stroma (Appleton et al., 2018). The propensity for melanoma to seed brain metastases suggests that melanoma in particular might be predisposed toward growing in soft environments (Achrol et al., 2019). Observing melanoma within *in vivo* mimetics, we observed both rounded and highly stretched cells (Figure 1A&B). This is in line with multiple reports of the remarkable morphological plasticity of melanoma, which shifts between a contractile rounded shape and a less contractile spread shape (Bergert et al., 2012; Sanz-Moreno et al., 2011, 2008). Numerous studies have documented the pro-migratory effect of intracellular contractility in melanoma (Gadea et al., 2007; Georgouli et al., 2019; Madsen et al., 2015; Orgaz et al., 2014; Sadok et al., n.d.; Sanz-Moreno et al., 2011), but it has remained unclear how these rounded cells actually move. Theoretical simulations of cell movement based on the assumption that cells use actomyosin contractility to form pressure-based protrusions suggest that this mode may be ideal for moving through stiff, disjointed 3D networks (Madsen et al., 2015; Tozluoğlu et al., 2013), yet the environmental obstacles used in these simulations are immobile, unlike the highly malleable fibers in unrestrained collagen networks.

Long-term time-lapse imaging of melanoma cells confirmed that rounded cells were able to move through our *in vivo* mimetics (Figure 1C). Although the movement was slower, it was more persistent than that of the stretched cells (Figure 1D&E). We confirmed that this rounded morphology phenotype was present *in vivo* using melanoma xenografts in zebrafish larvae (Figure 1F). These findings are in agreement with previous observations of rounded melanoma cells moving through Matrigel and in tumor xenografts in mice (Pinner and Sahai, 2008; Sahai and Marshall, 2003; Sanz-Moreno et al., 2011, 2008). They are also supported by histological analysis of melanoma in the tumor periphery, where a rounded morphology was found to be associated with cell invasion (Georgouli et al., 2019; Rodriguez-Hernandez et al., 2020).

We asked whether the rounded morphology was not only associated with the initial invasion, but more generally related to the metastatic potential of melanoma. To address this question, we imaged populations of primary melanoma cells with known *in vivo* metastatic potential. These cells were harvested from tumors in patients with stage III melanoma and then passaged in a mouse xenotransplantation system, in which the metastatic spread correlated with patient outcome (Quintana et al., 2012; Zaritsky et al., 2020). Across collagen microenvironments consisting of cells on top of a gel, cells in a restrained gel and cells in an unrestrained gel, the rounded morphology was enriched in the populations that exhibited higher metastatic efficiency (Figure 1G&H). A morphological feature that is strikingly revealed by our high resolution 3D microscopy is the prevalence of membrane blebs on these rounded cells. Blebs are small hemispherical protrusions that have been previously observed to co-occur with rounded morphologies of melanoma cells (Charras et al., 2005; Gadea et al., 2007) as well as certain cell lineages migrating *in vivo* (Kardash et al., 2010; Paluch and Raz, 2013). Comparing the morphologies

of a parental melanoma cell line (A375P) with a subpopulation of the cell line that has been enriched for its metastatic potential in a mouse model (A375M2) (Clark et al., 2000) revealed that the cell line with higher metastatic potential is selective for cells with a higher bleb count (Figure 1I&J). Thus, the rounded, blebby morphology observed in mechanically unrestrained collagen represents a physiologically relevant migration phenotype.

To examine the migration process in detail, we labeled the collagen with a fluorescent tag and used a computational 3D steerable filter to identify collagen fiber locations (Aguet et al., 2005; González et al., 2009; Jacob and Unser, 2004; Welf et al., 2016). Although the blebs were small enough to fit inside the pores in the collagen network, the nucleus and cell body of the rounded melanoma cells were much too large to fit through the existing pores (Figure 1K). This presents a puzzle: How do round cells that remain largely spherical migrate through a collagen network with pore sizes substantially smaller than their cell body?

Imaging the collagen in our *in vivo* mimetic samples after allowing the cells 24 hours to migrate, we found that many cells had created tunnels through the collagen (Figure 2A), in some cases leaving extracellular vesicles and retraction fibers stuck in the tunnels. These tunnels provide a forensic record of the migratory history of cells that move too slowly for the translocation to be detected over the time span of a high-resolution live-cell imaging experiment. We observed a similar tunneling phenomenon with a different melanoma cell line (Figure 2B), as well as with pediatric Ewing sarcoma cells (Figure 2C). This suggests that this tunneling capability is common to multiple cancer cell types.

Cancer cells can use extracellular matrix metalloproteases (MMPs) to create tunnels through dense matrices (Kessenbrock et al., 2010). To test whether melanoma tunneling was associated with MMP activity, we applied a broad spectrum MMP inhibitor, GM6001. Surprisingly, inhibitor treatment did not have any effect on the ability of melanoma cells to dig tunnels through collagen (Figure 2D). MMP inhibition had no effect on tunneling through collagen irrespective of whether the collagen was solubilized using pepsin, which removes a crosslinking site and results in softer collagen gels. We confirmed that GM6001 inhibited MMP activity under these conditions by imaging collagen that was cleaved at a specific residue by MMPs using a ¾ collagen antibody (Figure 2E), as well as by direct measurement of enzymatic activity. Quantifying the amount of ¾ collagen antibody staining inside tunnels under MMP inhibition showed that GM6001 eliminated collagen cleavage at the MMP site despite no change in tunneling (Figure 2F). Thus, we conclude that tunneling is not mediated enzymatically by MMPs.

The observation that tunneling frequency was reduced in unpepsinized collagen (Figure 2D) provides additional mechanistic insight into the process of worrying. Because some cell types are able to migrate through dense ECM despite MMP inhibition, it has been proposed that cells are able to squeeze through existing pores (Wolf et al., 2003). We measured the pore sizes of pepsinized and unpepsinized collagen networks and found that unpepsinized collagen gels had larger pore sizes (Figure 2G). If larger pores enabled more efficient migration as observed in mechanically restrained collagen (Wolf et al., 2013), then we would expect more frequent tunneling through unpepsinized gels. On the contrary, we find less tunneling in unpepsinized collagen, which suggests that the greater stiffness of unpepsinized collagen (advancedbiomatrix.com) is responsible for the reduced tunneling efficiency in unpepsinized gels. Although we cannot rule out the possibility that tunneling is reduced in unpepsinized gels because the stiffer gel encourages an alternative migration mode. Tunnels generated by cells in unpepsinized collagen gels showed evidence that the thicker collagen fibers in unpepsinized collagen gels were dragged along

as cells tunneled through the network (Figure 2H). This process manifests in collagen fiber organization as cells persistently migrate and create organized collagen patterns in their wake. We quantified collagen fiber orientation via the nematic order parameter measured relative to the mean fiber direction in the image. A mean nematic order parameter of 1 indicates fiber alignment, whereas 0 indicates no overall alignment. We found that tunnels formed by cells in unpepsinized gels showed greater collagen fiber alignment than tunnels formed by cells in pepsinized gels (Figure 2I). Altogether, these results suggest that tunneling is a mechanical process that is very different from the squeezing mode proposed previously as an MMP-independent motility process.

To elucidate how cells tunnel, we next analyzed the detailed interactions of cells with collagen. Cells inside tunnels are often highly polarized, with many large blebs at the cell front facing the tunnel front wall, and only small blebs facing the tunnel opening at the back of the cell (Figure 3A). We used an automated 3D morphological motif detector to delineate blebby and non-blebby regions of the cell surface (Driscoll et al., 2019). Measuring the difference in frequencies of protrusive and retractive motion on and off blebs, we found that blebs were on average protrusive and non-blebs retractive (Figure 3B), suggesting that blebs enable forwards cell movement in this tunneling migration mode. We next asked how blebs might be pushing through the dense collagen matrix. Using the motif detector to identify individual blebs and the steerable filter to detect collagen fibers, we found that collagen is enriched in regions near blebs, but not directly on blebs (Figure 3C). Careful inspection of the 3D images revealed why this is the case: Blebs interdigitate into pores in the collagen network, resulting in high collagen fiber density at the base of blebs (Figure 3D). Next, we examined the motion of the collagen network, revealing movement of individual collagen fibers at the front of tunneling cells (Figure 3E&F). Using a 3D optical flow algorithm designed to capture multi-scale motion both near and away from cells (Manandhar et al., 2020), we quantified the magnitude of collagen network motion (Figure 3G). We then compared the collagen speed near blebs with the bleb speed for both protruding and retracting blebs (Figure 3H). For protrusive blebs, we found that at low bleb speeds, collagen speed increases linearly with bleb speed, consistent with a regime in which the expanding bleb pushes collagen away from the cell. At high bleb speeds, however, collagen motion plateaus, consistent with a regime in which blebs snake into collagen pores, jittering collagen to the same extent regardless of their speed. Analyzing retractive blebs, we similarly found that at low bleb speeds, collagen speed increases linearly with bleb speed. However, at high speeds of retraction, we observed only a partial switch to an interdigitation regime. Taken together, this suggests that protruding blebs extend into collagen pores, but retracting blebs pull collagen towards the cell surface.

We observed that many highly polarized cells inside tunnels exhibited extensive internalization of labeled collagen at the cell front (Figure 3I). These blebby regions were often associated with enrichment of collagen into a shell at the cell periphery (Figure 3J). Over long periods of time, cells slowly agitated the collagen shell, breaking off fragments of the collagen and pulling them into the cell (Figure 3K). We asked what mechanism cells use to internalize the collagen and found that high molecular weight dextran was ingested alongside labeled collagen (Figure 3L). Internalization of large liquid-phase molecules is indicative of macropinocytosis (Kerr and Teasdale, 2009). Consistent with this conjecture, inhibiting macropinocytosis by the sodium hydrogen exchange inhibitor 5-(N-ethyl-N-isopropyl)amiloride (EIPA) (Masereel et al., 2003) decreased the apparent number of dextran-labeled vesicles and internalized collagen particles (Figure 3M). We confirmed this observation by automatically detecting internalized collagen particles using a multi-scale stochastic filter (Figure 3N) (Isogai et al., 2019). Furthermore, in EIPA-treated cells the number of internalized dextran vesicles and collagen particles were highly correlated

(Figure 3O), providing more evidence that dextran vesicle and collagen fragment internalization are coupled processes. As a further test, we calculated for each cell the likelihood that collagen localization at detected dextran vesicles was higher than expected by chance. We found that the distribution of p-values of a statistical test under the null hypothesis that the collagen particles are random was heavily tilted towards small values (Figure 3P), again consistent with collagen fragment internalization within dextran-filled vesicles. Altogether, these results suggest that blebs repeatedly agitate collagen at the closed end of the tunnel, pulling fibers towards the cell surface followed by slow internalization in order to clear space for cell movement.

We next asked how blebs and the internalization machinery might be polarized at the closed end of the tunnel. Polarization is essential to worrying since it enables persistent agitation necessary for the abrogation of the collagen network. We noted that the large blebs at the cell front were almost always oriented toward the closed end of the collagen tunnel (Figure 4A). To measure the polarization of large blebs, as well other data associated with the 3D cell surface, we mapped surface data to a sphere and fit it to a weighted von Mises distribution (Figure 4B). This distribution can be interpreted as a spherical normal distribution, with fit parameters intuitively corresponding to the direction of the peak and the peak's inverse width, which we here termed the polarization magnitude. Comparing the distributions of polarization magnitudes for large blebs and all blebs on each cell, we found that large blebs were more polarized (Figure 4C). An obvious cue that is present at the closed end of the tunnel and not the open end is the collagen itself. Comparing the direction of large bleb polarization with the mean direction of collagen localization near the cell surface, we found that large blebs were systematically biased towards areas of high collagen density (Figure 4D). We next wondered what mechanisms might be responsible for the selective organization of large blebs near regions of high-collagen density. We found that the shell of collagen at the closed end of the tunnel supported formation of paxillin-containing adhesion complexes (Figure 4E &F). Indeed, quantification confirmed that these complexes were highly polarized in the direction of the closed end of the tunnel (Figure 4G). Phosphoinositide 3-kinase (PI3K) is a canonical cell polarity factor that is organized by nascent adhesions via focal adhesion kinase (FAK) (Chen and Guan, 1994; Johnson et al., 2015; Welf et al., 2012), and in worrying cells, we observed a striking polarization of PI3K in the direction of the closed end of the tunnel (Figure 4H). This is somewhat surprising given that fibroblasts exhibiting pseudopodial motility in 3D microenvironments do not seem to require polarized PI3K signaling (Petrie et al., 2012). Moreover, PI3K signaling is more directionally aligned with large blebs than with blebs of all sizes (Figure 4I), suggesting that PI3K signaling is involved in the polarization of large blebs. Despite their small size, we found that adhesions in the cortical area of a worrying cell persisted for several minutes (Fig 4J), in contrast to the ~ 1 min lifetime of the similarly-sized nascent adhesions formed in cells on a coverslip (Choi et al., 2008). In regions of rapid protrusion, cells exhibited less persistent adhesions reminiscent of classical nascent adhesions (Fig 4K&L). The stability of the cortical adhesions may enable them to recruit PI3K to the front of worrying cells.

To test this hypothesis, we acutely inhibited FAK signaling using a small molecule inhibitor of FAK-kinase activity and measured the resulting changes to bleb volume, polarization and number, as well as PI3K polarization and mean cell surface motion. FAK inhibition resulted in a decrease in bleb volume, even though bleb polarization and number were unaffected. PI3K polarization and mean cell surface motion were also decreased (Figure 4M&N). Measuring the full-width half-maximum of the FAK inhibition response time, we found that PI3K polarization fell first, followed by bleb volume and then cell surface motion, suggesting that PI3K polarity is upstream of large bleb formation at the cell front (Figure 4M).

Consistent with this conjecture, we frequently observed that hot spots of PI3K intensity were associated with large blebs (Figure 5A). Automatically stratifying blebs by volume revealed that large blebs in particular were enriched for high PI3K signaling (Figure 5B). Large blebs were also associated with increased collagen motion (Figure 5C), suggesting that these large blebs are important for worrying. To determine if the relationship between PI3K and bleb size was causative, we used photoactivation to increase PI3K signaling locally in blebbing cells. This PI3K stimulation resulted in a striking local increase in bleb size in the region of PI3K activation (Figure 5D), which was found only in the region of photoactivation (Figure 5E). Next, we pharmacologically inhibited PI3K signaling in worrying cells. This resulted in a rapid decrease in PI3K biosensor intensity in the region formerly marked by high PI3K activity (Figure 5F) and an immediate decrease in bleb size in the same region. As shown by the time-lapse data following PI3K inhibition, de novo bleb formation was not inhibited. Aggregating such PI3K inhibition experiments over multiple cells, we found that both PI3K polarization and bleb size were decreased by PI3K inhibition, whereas the number of blebs and bleb polarization was not affected (Figure 5G). Altogether, these results indicate that PI3K is responsible for generating large blebs, but it does not determine the frequency or location of bleb initiation.

We next asked if the presence of large blebs affected PI3K activity. To address this, we perturbed cell blebbing directly via addition of wheat germ agglutinin (WGA), which reduces blebbing by binding to sialic acid and N-acetylglucosaminyl residues on the extracellular surface of the cell membrane, thereby increasing membrane stiffness (Charras et al., 2005; Evans and Leung, 1984). We found that decreasing bleb abundance via WGA decreases the polarity of PI3K signaling (Figure 5H&I). Hence, bleb abundance contributes to local PI3K activity. Comparison of the intensity decrease in either the non-blebby membrane or the cytosol confirmed that this PI3K signal decrease was not due to photobleaching of the biosensor (Figure 5J). The rate of PI3K decrease after WGA addition was substantially slower than the PI3K decrease following PI3K inhibition. The PI3K biosensor reports concentration of PI3K products (Haugh et al., 2000). Therefore, the different kinetics of PI3K inhibition via direct vs indirect inhibition through blebs suggest the existence of a feedback or diffusion trap for PI3K products rather than a role of blebs as a direct biochemical regulator of PI3K activity. Such a feedback would promote the formation of local PI3K hotspots (Figure 5L).

Blebs are understood to form via separation of the plasma membrane from the actin cortex and grow via cytoplasmic flow driven by intracellular pressure (Cunningham, 1995). In contrast, PI3K has been found to drive actin-dependent protrusion (Devreotes and Horwitz, 2015; Funamoto et al., 2002). Yet actin is thought to enter a bleb only to reform the actin cortex after it has stopped growing (Charras et al., 2006). Thus, the involvement of PI3K in bleb expansion seemed paradoxical. We noted, however, that PI3K and actin were frequently enriched in the same blebby regions (Figure 6A), and our 3D polarization analysis confirmed that PI3K and actin were directionally correlated (Figure 6B). We also found that regions of the cell with higher PI3K activity protrude faster (Figure 6C), suggesting that faster growth may be contributing to the larger blebs found in PI3K high regions. Indeed, in agreement with previous findings (Cunningham, 1995), we found that blebs that ultimately reach a larger size do so by growing faster (Figure 6D). Inhibition of PI3K activity dramatically decreased the growth rate and final bleb size (Figure 6D), confirming that this fast bleb growth and large size are due to PI3K signaling.

Based on these results, we wondered if there could be a role for actin polymerization during bleb expansion. Indeed, imaging cells expressing low levels of a HALO-tagged form of monomeric actin showed that G-actin is present during bleb expansion (Figure 6E). In contrast, the F-tractin construct, which

localizes to filamentous actin (Schell et al., 2001), was absent during bleb expansion and localized only to the bleb cortex, as previously reported (Charras et al., 2006). Calculating the ratio of monomeric actin to F-tractin allowed us to determine if monomeric actin is enriched in any regions relative to filamentous actin as measure by F-tractin. Averaging this calculation over the surfaces of multiple cells revealed that monomeric actin was enriched in blebs relative to filamentous cortical actin present on the cell surface outside blebs (Figure 6F), suggesting that monomeric or other forms of actin that are not detectable by F-tractin play a role in bleb expansion. Furthermore, stratification of different blebs by their final size revealed that larger blebs contain significantly more monomeric actin than small blebs, in particular later in their life (Figure 6G). To determine if actin polymerization is responsible for bleb growth, we inhibited WAVE-mediated dendritic actin polymerization with the Arp2/3 inhibitor CK666 (Bisi et al., 2013; Nolen et al., 2009). Inhibiting Arp2/3 decreased bleb volume, but, notably, did not systematically alter the number of blebs (Figure 6H &I), suggesting that dendritic actin polymerization may be responsible for growth of large blebs.

The GTPase Rac1 is activated by PI3K products (Chen and Guan, 1994; Welch et al., 2003) and activates WAVE (Chen et al., 2017), so we conjectured that Rac1 could be the critical intermediary between PI3K signaling and bleb expansion required for worrying. To test this hypothesis, we employed a photoactivatable Rac1 construct (Wu et al., 2009), which allowed us to increase Rac1 activity locally and acutely, largely avoiding compensation and global morphological effects. Local photoactivation of Rac1 in blebbing cells resulted in a dramatic, reproducible increase in local bleb size that was immediately reversible upon light cessation (Figure 6A&B). Taken together, these results show that the mechanism by which PI3K localization facilitates bleb growth is via Rac1-mediated actin polymerization.

Discussion

Our results define mechanical worrying as a cell migration mode that comes into effect in the previously unexplored regime of dense but very soft microenvironments, such as those encountered in the brain or bone marrow, but also locally in organs with composite tissue properties such as the liver or lymph nodes. By combining pressure-based blebs with actin-driven membrane expansion, mechanical worrying allows large cancer cells to move through dense microenvironments without extracellular proteases. The mechanism by which cells accomplish this involves a surprising role for membrane blebs in targeted mechanical degradation of ECM that facilitates internalization of ECM components via macropinocytosis. This ECM degradation depends upon the persistence of an overwhelming number of blebs punching, rubbing, and abrading against the extracellular mass – by our estimation a cell exerts on the order of 100,000 blebs over the course of 24 hours. Our data demonstrates this process within *in vivo* mimetic collagen gels. In a configuration reminiscent of the pictures shown in (Buehler, 2006) bleb-based agitation wears away concentric layers of collagen fibers, ultimately enabling their rupture and engulfment, which gives way to persistent migration.

Rounded cells typically exhibit less adhesive force than stretched cells (Jannat et al., 2011) and exhibit less dependence upon adhesion receptors (Boekhorst et al., 2020; Liu et al., 2015; Maaser et al., 1999). Nonetheless, our data revealed the formation of small, but biochemically functional adhesions between the agitating blebs at the cell front, as well as near the actin cortex. Formation of these adhesions at the closed front end of a collagen tunnel polarizes cells via biased adhesion formation and subsequent PI3K signaling, enabling them to maintain directional persistence of worrying indefinitely despite the short lifetime of a single bleb. The whole-cell motion supported by worrying is slow relative to the timescales accessible to time-lapse microscopy, which is likely one of the reasons this migration modality had been

missed in previous studies. Another reason is that worrying only happens in mechanically unrestrained environments. Thus, the migration mode is suppressed near a hard surface, which is common in most experimental set-ups for high-resolution live-cell microscopy. To discover worrying, we needed specialized imaging approaches that preserved the compliance of unrestrained environments (Welf et al., 2016).

Because cells are able to maintain persistent polarity, worrying cells may be able to travel large distances despite their slow speed. The finding that these biased adhesions lead to polarized PI3K signaling, combined with the well-established role of PI3K in other types of migration (Andrew and Insall, 2007; Welf et al., 2012; Zhan et al., 2020) suggests that PI3K might be a universal polarity factor in phenotypically diverse migration modes. This would enable cells to switch motility modes depending on the microenvironment without having to switch regulatory mechanisms or continuously organize multiple regulatory pathways (Bergert et al., 2012).

Our data indicates that the process of bleb initiation is independent of PI3K signaling. Rather, bleb formation is initiated randomly by the combination of membrane cortex detachment and intracellular pressure (Charras et al., 2008; Diz-Muñoz et al., 2010). This implies that persistent polarization of large blebs, which is essential to the worrying process, is governed by pathways, which enforce growth in a spatially polarized fashion. The mechanistic distinction between bleb initiation and growth shares striking parallels to initiation and growth of lamellipodial protrusions (Welf et al., 2012). We recently reported that initiation of lamellipodial protrusions first requires actin-membrane release, followed by an increase in local actin polymerization to reinforce lamellipodial expansion under the control of Rac1 signaling (Welf et al., 2019). Thus, in addition to their use of the PI3K/Rac1/actin pathway, the two seemingly disparate processes of bleb-based and lamellipodial protrusions follow similar initiation and growth paths.

One of the most surprising discoveries in the presented experiments is indeed the role for actin polymerization in the enlargement of worrying blebs. Bleb expansion is commonly thought to be promoted by intracellular pressure. According to this view, actin filament assembly occurs only at late stages to provide a substrate for myosin motor-based retraction of the bleb and reintegration with the greater actin cortex and membrane system. We show by direct inhibition or activation of actin polymerization that actin filament growth is required also during bleb expansion. What exactly is the role of actin polymerization during bleb growth? In lamellipodial protrusion, actin polymerization is thought to generate force necessary for membrane advancement. Conceivably, the same mechanism could be at play in the bleb. Actin filament polymerization against the inner membrane of an expanding bleb could support pressure-based expansion, producing the faster growing, larger and presumably also more forceful, blebs responsible for worrying. Alternatively, actin polymerization inside the bleb could also serve to very locally control pressure generation. Figuring out which of these two possibilities dominates will require an in depth analysis of the fluid flows inside individual blebs. It has been shown that membrane availability also affects bleb size and expansion speed (Goudarzi et al., 2017). Yet, it is not clear how actin polymerization would modulate membrane availability. Regardless of the precise mechanism, the involvement of an active process like actin polymerization, rather than only pressure-based expansion, offers the opportunity for the cell to regulate the location and magnitude of bleb growth via intracellular signaling. Our data shows that because of the dependence on actin assembly, the spatial organization of worrying blebs is under the control of PI3K/Rac signaling, which ensures persistent blebbing at the cell front as the characteristic feature of worrying.

A hallmark of worrying migration is the ability of cells to continuously remove the fractured ECM components at the cell front. Our experiments revealed that macropinocytosis is the primary mechanism of debris collection. This observation reinforces previous observations that macropinocytosis can take up ECM (Yamazaki et al., 2020), although to our knowledge it has not been reported that ECM uptake is involved in persistent cell migration. We and others find that the persistently round morphology of worrying cells is enriched in highly metastatic populations (Georgouli et al., 2019). Given that the cellular pathways that regulate macropinocytosis are also enriched in metastatic cancer cells, our findings document a previously underappreciated function for macropinocytosis in metastasis beyond the well-established nutrient uptake (Recouvreux and Commisso, 2017). Because the pathways that mediate macropinocytosis - notably PI3K and Rac1 - are the same pathways that regulate cytoskeletal remodeling during worrying, worrying cells do not require any additional polarization cues. In contrast, it is not clear if or how MMP-mediated matrix degradation may be polarized in the direction of cell migration (Kessenbrock et al., 2010). Furthermore, excretion of soluble MMPs would create a gradient surrounding the cell and would actually degrade the matrix at the sides of a cell, which may be needed for generating the traction needed for whole-cell motion. There is some evidence that adhesion receptors may regulate MMP localization (Wolf et al., 2007), but specific degradation of soft ECM at the points of adhesion would untether the cell and render it incapable of applying force to the ECM. Thus, given that cells exhibit the stretched morphology when engaged in MMP-driven 3D migration (Wolf et al., 2003; Wyckoff et al., 2006) and that melanoma cells exhibit the stretched morphology in mechanically restrained microenvironments (Welf et al., 2016), it is tempting to speculate that that the role of MMPs in stiff environments may not be to remove ECM, but simply to soften it enough for allowing cell passage (Ferrari et al., 2019).

In summary, the hallmarks of worrying are actin-dependent polarized bleb growth, MMP-independent movement through soft ECM, and polarized macropinocytic uptake of fractured ECM at the cell front. This combination of features illustrates the many ways that cells can organize cytoskeletal dynamics to move through diverse microenvironments. The preference of cells to use worrying to move through soft, mechanically unrestrained ECM suggests that it may be adopted by cells that migrate through acellular tissues, such as those at the periphery of tumors (Georgouli et al., 2019). This raises the possibility that worrying might be a more targetable process for preventing metastatic spread than MMP inhibition.

Methods

Cell culture and reagents

MV3 cells were obtained from Peter Friedl (MD Anderson Cancer Center, Houston TX). A375 (ATCC® CRL-1619) and A375MA2 (ATCC® CRL-3223) cells were acquired from ATCC. SKNMC Ewing sarcoma cells were obtained from the Whitehurst lab at UT Southwestern. MV3, A375, and SKNMC cells were cultured in DMEM (Gibco) supplemented with 10% fetal bovine serum (FBS; ThermoFisher) at 37 ^{o}C and 5% CO_2.

Inhibitors

FAK inhibitor 14 was purchased from Tocris (3414). PI3K alpha inhibitor IV was purchased from Santa Cruz (sc-222170). CK666 was purchased from Millipore Sigma (SML0006). The ¾-collagen antibody was purchased from Adipogen (AG-25T-011). NEIPA was purchased from Sigma (A3085). WGA was purchased from VWR (101098-084). 70 kDa Fluorescein isothiocyanate–dextran was purchased from Sigma (46945). GM6001 was purchased from Sigma (CC1010).

MMP activity assay

We used the MMP activity assay kit from abcam (ab112146) according to their instructions. MV3 melanoma cells were cultured in a 24 well plate with (a) media with no cells, (b) cells treated with vehicle (DMSO) control, and (c) cells treated with GM6001 for 24h. Two positive controls of recombinant human MMP1 and MMP8 from RnD systems (901-MP & 908-MP) were used for the assay. The control MMPs were dissolved in assay buffer and a 2mM AMPA working solution was prepared with assay buffer. The MMP and the test samples were mixed 1:1 vol/vol with the AMPA working solution and incubated for 1h at 37 ^{o}C. The MMP green substrate working solution was prepared in assay buffer and then mixed 1:1 vol/vol in the black walled 96 well plate and further incubated for 1h. The samples were then read on a Biotek, Synergy H1 hybrid plate reader at Ex/Em = 490/525 nm.

Recombinant DNA Constructs

The GFP-AktPH construct was obtained from the laboratory of Jason Haugh (North Carolina State University, Raleigh NC) (Haugh et al., 2000) and cloned into the pLVX-IRES-puro vector (Clontech). The GFP-tractin construct was a gift from Dyche Mullins (Addgene plasmid # 58473; http://n2t.net/addgene:58473; RRID:Addgene_58473) (Belin et al., 2014) and was cloned into the pLVX-IRES-puro vector (Clontech). Paxillin-pEGFP was a gift from Rick Horwitz (Addgene plasmid # 15233 ; http://n2t.net/addgene:15233; RRID:Addgene_15233) (Laukaitis et al., 2001). Cells expressing lentiviral vectors were created by following the manufacturer's instructions for virus preparation and cell infection (Clontech). Cells were selected for expression by treatment with puromycin, G418, or by using fluorescence activated cell sorting.

The photoactivatable PI3K construct (Idevall-Hagren et al., 2012) was created by cloning mCherry-CRY2-iSH2 (Addgene Plasmid #66839) into the pLVX-neo vector (Clontech). The CIBN-CAAX plasmid was obtained from Addgene (Plasmid #79574) and cloned into the pLVX-puro vector. Cells expressing both the mCherry-CRY2-iSH2 and the CIBN-CAAX constructs were selected by treatment with 10 mg/mL puromycin and fluorescence activated cell sorting. It is critical for the two part cry2 photoactivation system that cells express sufficient concentration of the CIBN-CAAX construct or the cry2 construct will aggregate in the cytosol instead of being recruited to the membrane. Thus, the optimal ratio of CIBN:cry2 is greater than one; cells expressing insufficient CIBN-CAAX will not respond to light. We also noted through the course of our experiments that cells will stop expressing one or both of these constructs if not kept constantly under selective pressure. Such a loss of expression will result in non-responsive cells. The PA-Rac1 construct was obtained from Yi I. Wu (University of Connecticut Health Center, Farmington, CT).

Overexpression of fluorescently tagged monomeric actin can perturb cell cytoskeletal dynamics. To avoid this artifact while imaging tagged actin, we expressed HALO-tagged actin under the control of a truncated CMV promotor, which results in lower expression of tagged actin than the full length promoter. The original actin construct features an 18 amino acid linker between mNeonGreen and actin in a pLVX-shRNA2 vector and was obtained from Allele Biotech. We truncated the CMV promoter, and replaced the mNeonGreen fluorophore with the HALO tag sequence. The sequence of the CMV100 promoter region is as follows, with the CMV sequence highlighted and the Kozak and start codon in bold:

AGTTATTAATAGTAATCAATTACGGGGTCATTAGTTCATAGCCCATATATGGAGTTCCGCGTTACATAAC
TTACGGTAAATGGCCCGCCTGGCTGACCGCCGCTAGCGCTAACTAGT**GCCACCATG**

Phase-contrast imaging

Live-cell phase-contrast imaging was performed on a Nikon Ti microscope equipped with an environmental chamber held at 37°C and 5% CO_2 in 20x magnification.

Cells on top of gels

In order to prevent morphological homogenization and to better mimic the collagenous ECM of the dermal stroma, we imaged cells on top of a thick slab of collagen. Collagen slabs were made from rat tail collagen Type 1 (Corning; 354249) at a final concentration of 3 mg/mL, created by mixing with the appropriate volume of 10x PBS and water and neutralized with 1N NaOH. A total of 200 µL of collagen solution was added to the glass bottom portion of a Gamma Irradiated 35MM Glass Bottom Culture Dish (MatTek P35G-0-20-C). The dish was then placed in an incubator at 37°C for 15 minutes to allow for polymerization.

Cells were seeded on top of the collagen slab at a final cell count of 5000 cells in 400 uL of medium per dish. The dish was then placed in a 37°C incubator for 4 hours. Following incubation, 1 mL of medium was gently added to the dish. The medium was gently stirred to suspend debris and unattached cells. The medium was then drawn off and gently replaced with 2 mL of fresh medium.

Cells embedded in 3D collagen

Collagen gels were created by mixing bovine collagen I (Advanced Biomatrix 5005 and 5026) with concentrated phosphate buffered saline (PBS) and water for a final concentration of 2 mg/mL collagen. This collagen solution was then brought to pH 7 with 1N NaOH and mixed with cells just prior to incubation at 37°C to induce collagen polymerization. Cells were suspended using trypsin/EDTA (Gibco), centrifuged to remove media, and then mixed with collagen just prior to incubation at 37°C to initiate collagen polymerization. To image collagen fibers, a small amount of collagen was conjugated directly to AlexaFluor 568 dye and mixed with the collagen sample just prior to polymerization.

3D confocal imaging

The cell/collagen mixture described in the previous section was added to Nunc Lab-Tek II Chambered Coverglass samples holders with a No. 1.5 borosilicate glass bottom (Thermo Scientific). Cells were fixed with paraformaldehyde and stained with Hoechst and FITC-phalloidin. Images were acquired on a Zeiss LSM 880 using a Plan-Apochromat 63x/1.4 Oil objective.

Zebrafish injection and imaging

B16F10 melanoma cells expressing Lifeact-eGFP were injected into the hindbrain ventricle of 2 days post-fertilization wildtype zebrafish larvae using previously described methods (Roh-Johnson et al., 2017). Briefly, B16F10 melanoma cells were suspended in HBSS. 25-50 cancer cells were transplanted into the hindbrain ventricle of anesthetized larvae. Injected zebrafish larvae were incubated at 31°C with 0.2 mM PTU to prevent pigment formation. Live-cell *in vivo* imaging was performed using a Zeiss spinning disc microscope with a QuantEM EMCCD camera.

3D cell tracking from phase-contrast movies

Cells were embedded in 2.0 mg/mL pepsinized bovine collagen in Nunc Lab-Tek II Chambered Coverglass samples holders as described above. Live-cell phase-contrast imaging was performed on a Nikon Ti microscope as described above. Cells were outlined manually using ImageJ, and position and shape data were exported for analysis using Matlab. Cell shape was calculated using roundness, given by 4*area/(π*major_axis^2), and cells were classified as either round (roundness > 0.8) or stretched (roundness < 0.8). Autocorrelation was calculated using the Matlab function *xcorr*. Cell velocity was calculated from cell centroid positions.

3D light-sheet imaging

3D samples were imaged using either an axially-swept light-sheet microscope (Dean et al., 2016, 2015) or a meSPIM microscope (Welf et al., 2016), both of which provide nearly isotropic, diffraction-limited 3D images. Samples were imaged in phenol red free DMEM containing 25mM HEPES (ThermoFisher) with 10% FBS and antibiotic-antimycotic (Gibco), held at 37°C during imaging. Images were collected using sCMOS cameras (Orca Flash4.0 v2, Hamamatsu) and microscopes were operated using custom Labview software. All software was developed using a 64-bit version of LabView 2016 equipped with the LabView Run-Time Engine, Vision Development Module, Vision Run-Time Module and all appropriate device drivers, including NI-RIO Drivers (National Instruments). Software communicated with the camera via the DCAM-API for the Active Silicon Firebird frame-grabber and delivered a series of deterministic TTL triggers with a field programmable gate array (PCIe 7852R, National Instruments). These triggers included analog outputs for control of mirror galvanometers, piezoelectric actuators, laser modulation and blanking, camera fire and external trigger. All images were saved in the OME-TIFF format. Some of the core functions and routines in the microscope control software are licensed under a material transfer agreement from Howard Hughes Medical Institute, Janelia Research Campus.

3D cell image analysis

3D light-sheet images of cells were first deconvolved using a Richardson-Lucy algorithm. To reduce deconvolution artifacts, images were apodized, as previously described (Welf et al., 2016). Following deconvolution, we used our previously published u-shape3D analysis framework (Driscoll et al., 2019) to segment cells, detect blebs, map fluorescence intensity to the cell surface, measure surface motion, and calculate polarization statistics. Briefly, images of cells were segmented to create a cell surface represented as a 3D triangle mesh. We used u-shape3D's *twoLevelSurface* segmentation mode, which combines a blurred image of the cell interior with an automatically thresholded image of the cell surface. Blebs were detected by breaking the surface up into convex patches, and using a machine learning algorithm to classify the patches as a bleb or not a bleb. To measure the fluorescence intensity local to each mesh face, we used the raw, non-deconvolved, fluorescence image. At each mesh face, a kd-tree was used to measure the average pixel intensity within the cell and within a sampling radius of the mesh face. To correct for surface-curvature dependent artifacts, we depth normalized (Elliott et al., 2015) the image before measuring intensity localization by normalizing each pixel by the average pixel intensity at that distance interior to the cell surface. Polarization statistics were calculated by mapping data defined on the cell surface to a sphere, and fitting the mapped data to a 3D von Mises distribution, which is akin to a spherical normal distribution. The u-shape3D software, as well as the trained machine learning models used here, are available with the previously published manuscript (Driscoll et al., 2019).

Unlike in the published u-shape3D framework, we calculated bleb polarization by representing each bleb by the location on the bleb surface farthest from the bleb edge, with distances measured on the cell surface. Additionally, since the adhesion images had substantial fluorescence background, to measure adhesion polarization, we bandpass filtered the raw images via a difference of Gaussians procedure, selecting for objects between 1 and 6 pixels in radius.

3D collagen image analysis

To enhance linear image features, such as collagen fibers, the 3D collagen images were processed with a steerable filter of width 2 pixels, as previously described (Welf et al., 2016). To emphasize collagen fiber location, some figure panels, as indicated in the figure legends, show steerable-filter enhanced collagen. Other collagen images, especially those related to endocytosis, were neither steerable filtered nor deconvolved to avoid the creation of any artifacts. Collagen polarization near the cell surface was

measured after mapping image intensity values from steerable-filtered images onto the cell surface. Following steerable filtering and automatic thresholding, the nematic order parameter of collagen networks was calculated as described previously (Welf et al., 2016), except that the average fiber directionality in each 3D image was used as the reference direction. The fiber directionality was calculated at each voxel via a steerable filter. Collagen pore size analysis was also performed as described previously, (Lomakin et al., 2020) on steerable filtered and then thresholded images. To measure pore sizes, for each image, we fit the largest possible sphere into the collagen pores, fit the next largest possible sphere, excluding the volume of the previous sphere, and so on. Continuing fitting spheres until no remaining spheres above a size threshold would fit. We defined the distribution of collagen pore sizes as the distribution of fitted sphere diameters. Collagen motion was further measured using a previously published 3D optical flow algorithm (Manandhar et al., 2020). This algorithm combines a matching framework for large displacements across frames with a variational framework for small displacements. We mapped the magnitude of the collagen motion calculated via optical flow onto the cell surface, using the framework for mapping fluorescence intensity onto the cell surface described above.

3D dextran assay image analysis

To measure the endocytosis of collagen fragments alongside 70 kDa dextran, we first segmented the cell using the dextran channel. To do so, we inverted each 3D image, subtracted the median intensity, normalized by the 99th intensity percentile, subtracted the image background, thresholded, morphologically dilated by 1 pixel, morphologically eroded by 8 pixels, filled holes, and finally selected the largest image component. Since the cell is morphologically eroded to a greater extent than it is dilated, the cell segmentation is effectively shrunk, reducing the effect of segmentation errors on later analysis. To detect dots of endocytosed collagen and dextran, we employed a previously published multiscale stochastic filter (Isogai et al., 2019). For this filter, we used scales of 1.5 to 4 pixels, an $\alpha = 0.01$, and detected dots only inside the segmented cell. The p-value distribution shown in figure 3P results from testing, for each cell, the hypothesis that collagen fluorescence intensity is greater at the location of detected dextran dots than elsewhere in the cell. To calculate the p value for each cell, we randomly picked *n* collagen intensity values within the cell 100,000 times, where *n* is the number of detected dextran dots, and calculated the probability that the mean of the randomly picked values was greater than the mean of the collagen intensity values at the true detected dextran dots.

Photoactivation

Photoactivation of subcellular regions was performed using a 488 nm laser at 10% power via the FRAP module of a Zeiss LSM780 outfitted with temperature and CO_2 control. To assess bleb size change in phase contrast movies, we analyzed multiple blebs within the stimulated region by manually outlining individual blebs at their largest size using ImageJ. Bleb size was measured prior to activation and during activation in the same sub-region of the cell.

Visualization and Statistics

3D surface renderings were made in ChimeraX (Goddard et al., 2018). Colored triangle meshes representing the cell surface were imported into ChimeraX from u-shape3D as Collada dae files, as previously described (Driscoll et al., 2019). To render collagen, steerable-filtered images were opened directly in ChimeraX and thresholded. To create the rendering of adhesions shown in Figure 4F, the raw paxillin images were bandpassed, admitting objects between 0.5 and 3 pixels in radius, and then median filtered.

Figure 3H and 6I are histograms with varied bin sizes. To avoid the existence of bins with very little data, each bin in these panels contains a decile of data. Furthermore, to ease visual interpretation, the time series data in Figure 4M were smoothed using a moving average filter with a span of 5 frames.

All statistical comparisons shown in figures were calculated using a one-sided or two-sided t-test with α = 0.05. Error bars in figures show either 95% confidence intervals or the standard error of the mean, as stated in the figure legends. Number of cells and/or number of different experiments analyzed are given in the figure legends.

Acknowledgments

We thank Allan Zhang for manually tracking the cells imaged via phase-contrast microscopy, as well as Philippe Roudot for advice using the optical flow algorithm. Cell and collagen rendering performed with UCSF ChimeraX, developed by the Resource for Biocomputing, Visualization, and Informatics at the University of California, San Francisco, with support from National Institutes of Health R01-GM129325 and the Office of Cyber Infrastructure and Computational Biology, National Institute of Allergy and Infectious Diseases.

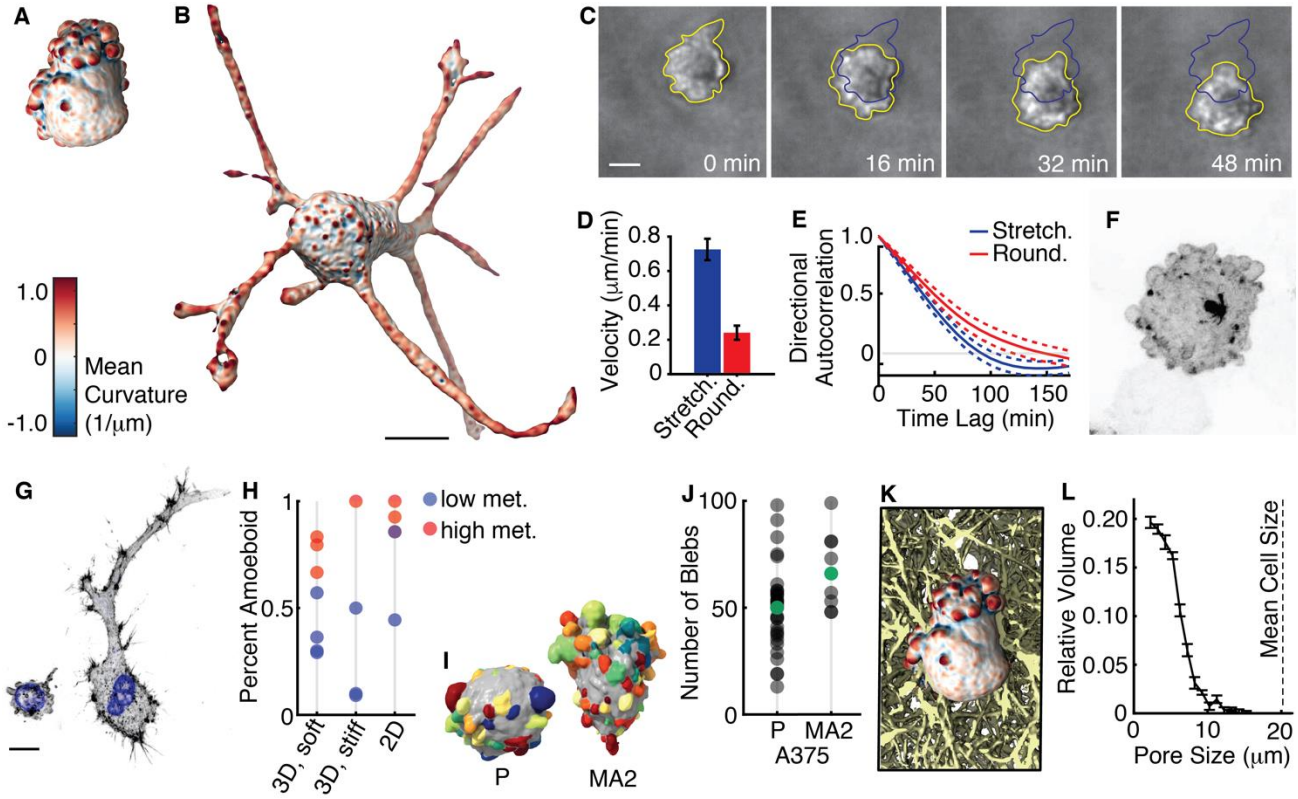

Figure 1. Round blebby cells are enriched in metastatic populations and exhibit slow but persistent migration through dense 3D matrix. (A&B) Surface rendering of a 3D light-sheet microscopy image of two different melanoma cell morphologies observed in 3D collagen. (C) Time-lapse phase-contrast microscopy images showing the movement of a round, blebby cell in 3D collagen. (D) Mean instantaneous velocity of melanoma cells in 3D collagen, separated by cell shape (n = 68 cells). (E) Directional persistence as measured by the directional autocorrelation of single cell trajectories, separated by cell shape (n = 68 cells). Greater lag times indicate more persistent migration. (F) Maximum intensity projection of a 3D confocal image of a B16 melanoma cell xenografted into a zebrafish embryo. (G) Maximum intensity projections of confocal images of melanoma cells in 3D collagen gels exhibiting amoeboid (left) and mesenchymal (right) morphologies. (H) Fraction of primary melanoma cells from xenografts categorized as high or low metastatic efficiency that exhibit amoeboid morphology under three different microenvironmental conditions. (I) Surface renderings of parental, P, and metastatic, MA2, A375 melanoma cells. Automatically identified blebs are shown randomly colored. (J) Number of blebs per cell in the parental, P, and metastatic, MA2, cells. Cells with the median number of blebs are indicated in green and shown in panel I. (K) Surface rendering of the melanoma cell shown in A along with the collagen fibers behind it in yellow. (L) Pore size analysis of 2.0 mg/ml bovine collagen gels showing the fraction of space occupied by a specific pore size (n = 6 gels). Error bars indicate the standard error of the mean. In comparison, the mean diameter of blebby melanoma cells in these types of gels is 20 ± 1 μm (n = 44 cells).

Figure 2. Round blebby cells do not require MMP activity to dig tunnels through dense 3D matrix

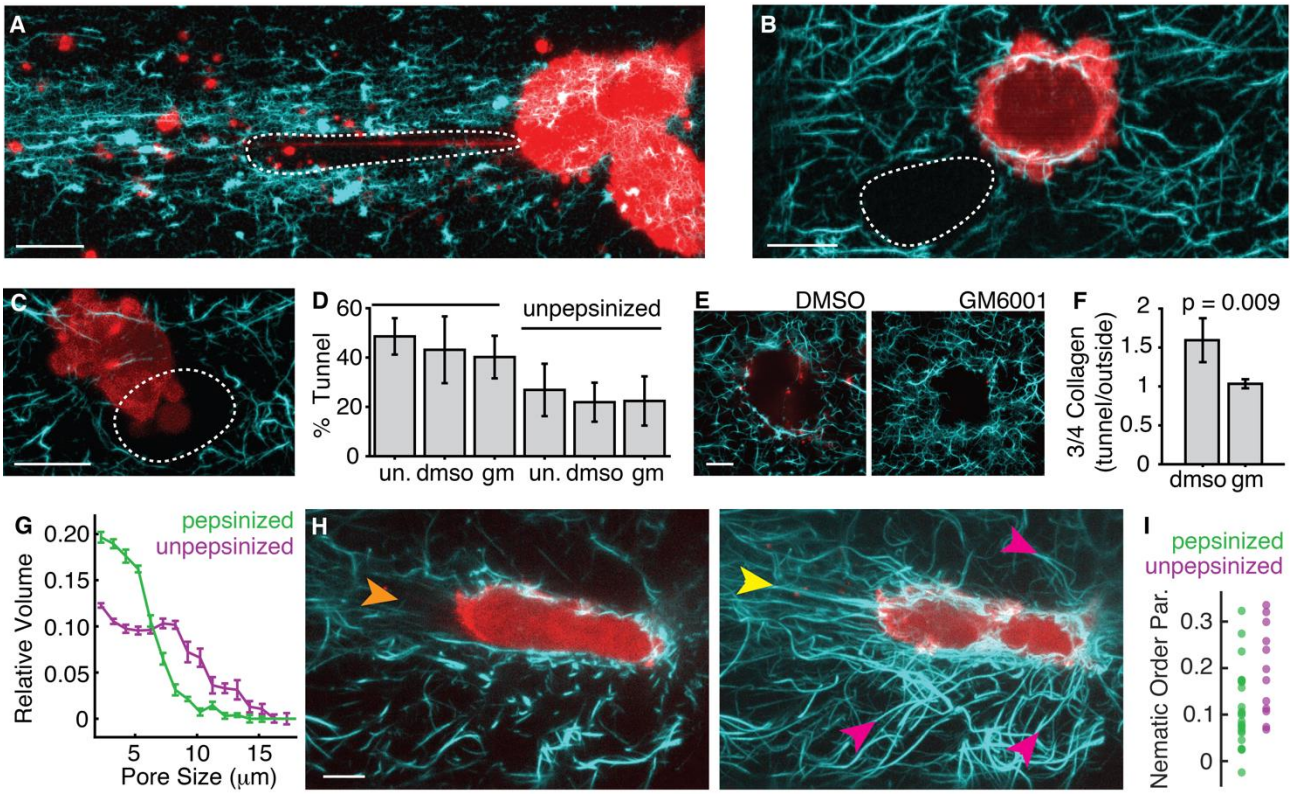

(A) Maximum intensity projection across 3.2 μm (20 slices) of a light-sheet microscope image of two MV3 melanoma cells expressing GFP-AktPH (red) in 3D collagen (cyan). The collagen image was processed with a computational filter to visually enhance fibers. The white dashed line indicates the location of a tunnel. (B) Maximum intensity projection across 4.8 μm of a light-sheet microscope image of an A375MA2 melanoma cell expressing GFP-F-tractin (red) in 3D collagen processed to enhance edges (cyan). The white dashed line indicates the location of a tunnel. (C) Maximum intensity projection across 18 μm of a light-sheet microscope image of an Ewing sarcoma cell expressing GFP-F-tractin (red) in 3D collagen with fibers computationally enhanced (cyan). The white dashed line indicates the location of a tunnel. (D) Percent of cells in tunnels after 18-24 hours in pepsinized or unpepsinized bovine collagen. Samples were either untreated (un.; n = 176 cells pepsinized, 67 cells unpepsinized), or treated with DSMO (n = 52 cells pepsinized, 105 cells unpepsinized), or 40 mM GM6001 (gm; n = 82 cell pepsinized, 67 cells unpepsinized). Error bars indicate 95% confidence intervals. (E) Single optical sections of 3D light-sheet images of collagen samples containing MV3 cells treated with either DMSO or 40 μM GM6001 for ~24 hours. The cyan channel shows collagen with fibers enhanced and the red channel shows ¾ collagen antibody fluorescence near tunnels formed by cells. (F) Quantification of ¾ collagen antibody intensity inside a tunnel divided by the intensity outside the tunnel in samples treated with either DMSO or 40 μm GM6001. Error bars show 95% confidence intervals with p = 0.009 (n = 4 tunnels for each condition). (G) Pore size analysis of pepsinized and unpepsinized 3D collagen samples. Error bars indicate the standard error of the mean (n= 6 gels per condition). The pepsinized data was shown in 1L. (H) Maximum intensity projections of a single light-sheet microscope image of an MV3 melanoma cell expressing GFP-AktPH (red) in pepsinized 3D collagen with fibers enhanced (cyan), projected across

1.1 μm (left) and 8.2 μm (right). The orange arrow indicates the tunnel formed by the cell, the yellow arrow indicates a collagen fiber being dragged behind the cell, and the magenta arrows indicate collagen fibers being dragged from the sides in the cell's wake. (I) Nematic order parameter quantifying the extent of collagen fiber alignment in images of pepsinized and unpepsinized 3D collagen containing cells ($p = 0.009$). All scale bars show 10 μm.

-

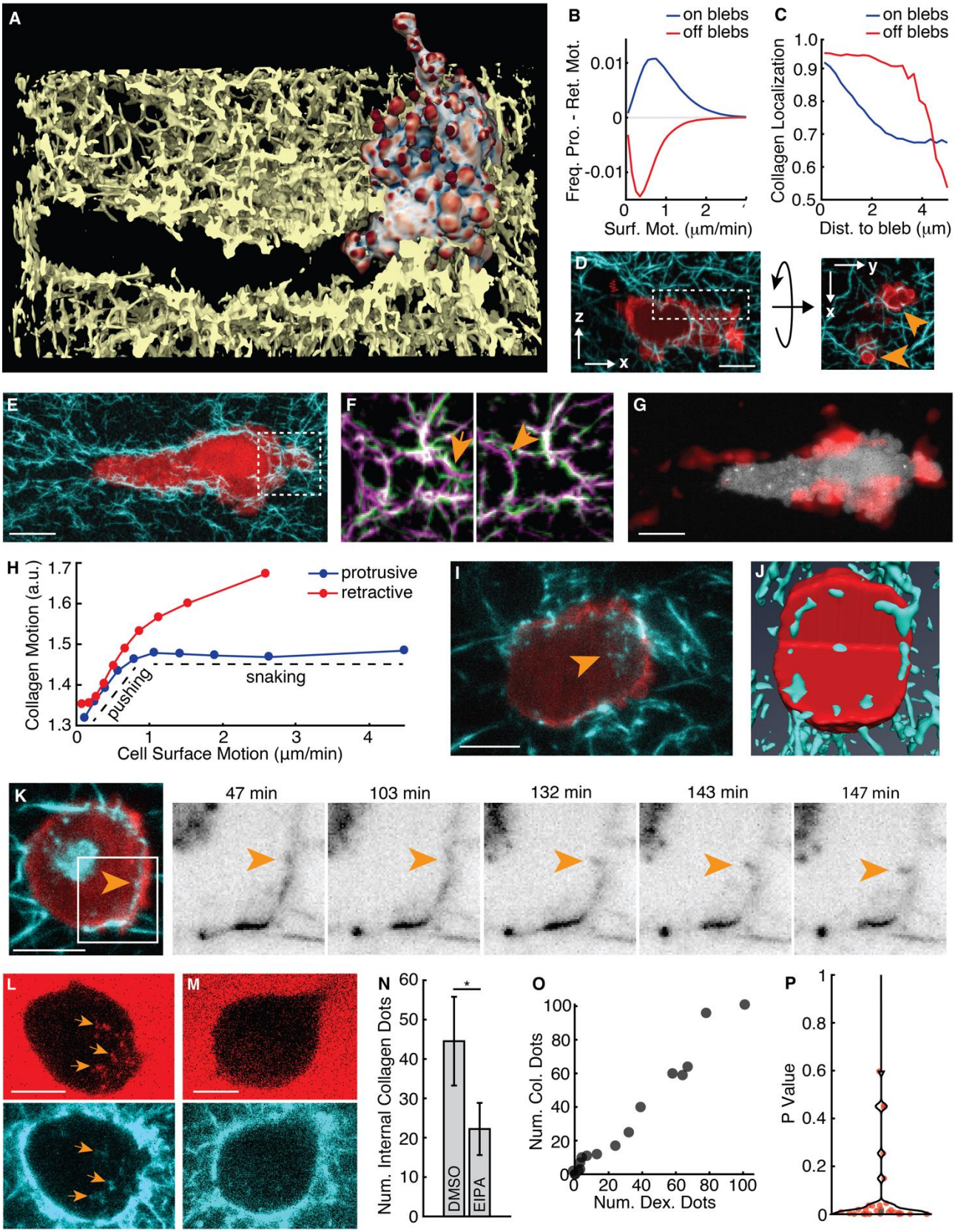
A
B
on blebs
off blebs
Freq. Pro. - Ret. Mot.
0.01
0
-0.01
0
1
2
Surf. Mot. (μm/min)
C
on blebs
off blebs
Collagen Localization
1.0
0.9
0.8
0.7
0.6
0.5
0
2
4
Dist. to bleb (μm)
D
z
x
y
x
E
F
G
H
Collagen Motion (a.u.)
1.7
1.6
1.5
1.4
1.3
protrusive
retractive
pushing
snaking
0
1
2
3
4
Cell Surface Motion (μm/min)
I
J
K
47 min
103 min
132 min
143 min
147 min
L
M
N
Num. Internal Collagen Dots
60
50
40
30
20
10
0
*
DMSO
EIPA
O
Num. Col. Dots
100
80
60
40
20
0
0
20
40
60
80
100
Num. Dex. Dots
P
P Value
1
0.8
0.6
0.4
0.2
0

Figure 3. Mechanical worrying employs persistent agitation and internalization of collagen to dig tunnels. (A) Surface rendering of a light-sheet microscope image of an MV3 melanoma cell, colored by surface curvature, in 3D collagen. The scale for surface curvature is shown in Figure 1C. (B) The frequency of protrusive motion minus the frequency of retractive motion on and off blebs (n = 9 cells). (C) Collagen intensity on and off blebs as a function of distance to the nearest bleb edge (n= 23 cells). (D) XZ and XY views of maximum intensity projections of light-sheet images of a melanoma cell expressing GFP-AktPH (red) interacting with collagen fibers with edges enhanced (cyan) projected over 5.6 μm and 2.4 μm, respectively. The region shown in the XY view is indicated by the dashed box in the XZ view. Orange arrows indicate blebs interdigitating between collagen fibers. (E) Maximum intensity projection across 3.2 μm of a light-sheet image of a melanoma cell expressing GFP-AktPH (red) in 3D collagen with edges enhanced (cyan). The dashed box indicates the region magnified in panel F. (F) Overlay of two different time points (green and magenta, separated by 120 seconds) of a maximum intensity projection over 3.2 μm of a light-sheet microscope image of collagen with edges enhanced. Orange arrows indicate the motion of individual collagen fibers. (G) Collagen motion (red), as measured by 3D optical flow, near a melanoma cell expressing GFP-AktPH (white), imaged using light-sheet microscopy and shown as a maximum intensity projection over the entire cell. (H) Collagen motion near the cell surface as a function of either protruding blebs (blue) or retracting blebs (red) imaged using light-sheet microscopy (n = 5 cells). (I) Maximum intensity projection across 3.2 μm of a light-sheet image of a cell expressing GFP-AktPH (red) in 3D collagen (cyan). The orange arrow indicates internalized collagen at the front of the cell. (J) Surface rendering of a light-sheet microscopy image of a melanoma cell expressing GFP-AktPH (red) in 3D collagen (cyan). A quadrant of the cell and collagen is cut away to show collagen internalized at the cell periphery. (K) Maximum intensity projection across 3.2 μm of a light-sheet microscope image of a cell expressing GFP-AktPH (red) in 3D collagen (cyan). The dashed box indicates the region magnified in the time-lapse panels to the right and the orange arrow indicates a piece of collagen that is broken off and brought in towards the center of the cell. (L&M) Maximum intensity projection across 3.2 μm of a light-sheet microscope image of MV3 cells (unlabeled) in 3D collagen (cyan) treated with 70kDa FITC-dextran (red), as well as either DMSO (L) or 50 mM EIPA (M). The orange arrows indicates internalized collagen and dextran in intracellular vesicles. (N) Number of internalized collagen fragments in either DMSO (n = 20 cells) or EIPA-treated (n = 23 cells) cells (p = 0.04) (O) Number of internalized collagen fragments per cell vs. the number of internalized dextran dots in EIPA-treated cells. (P) The p value, calculated for each cell, corresponding to the likelihood that collagen fluorescence intensity is elevated at the location of dextran dots. All scale bars show 10 μm.

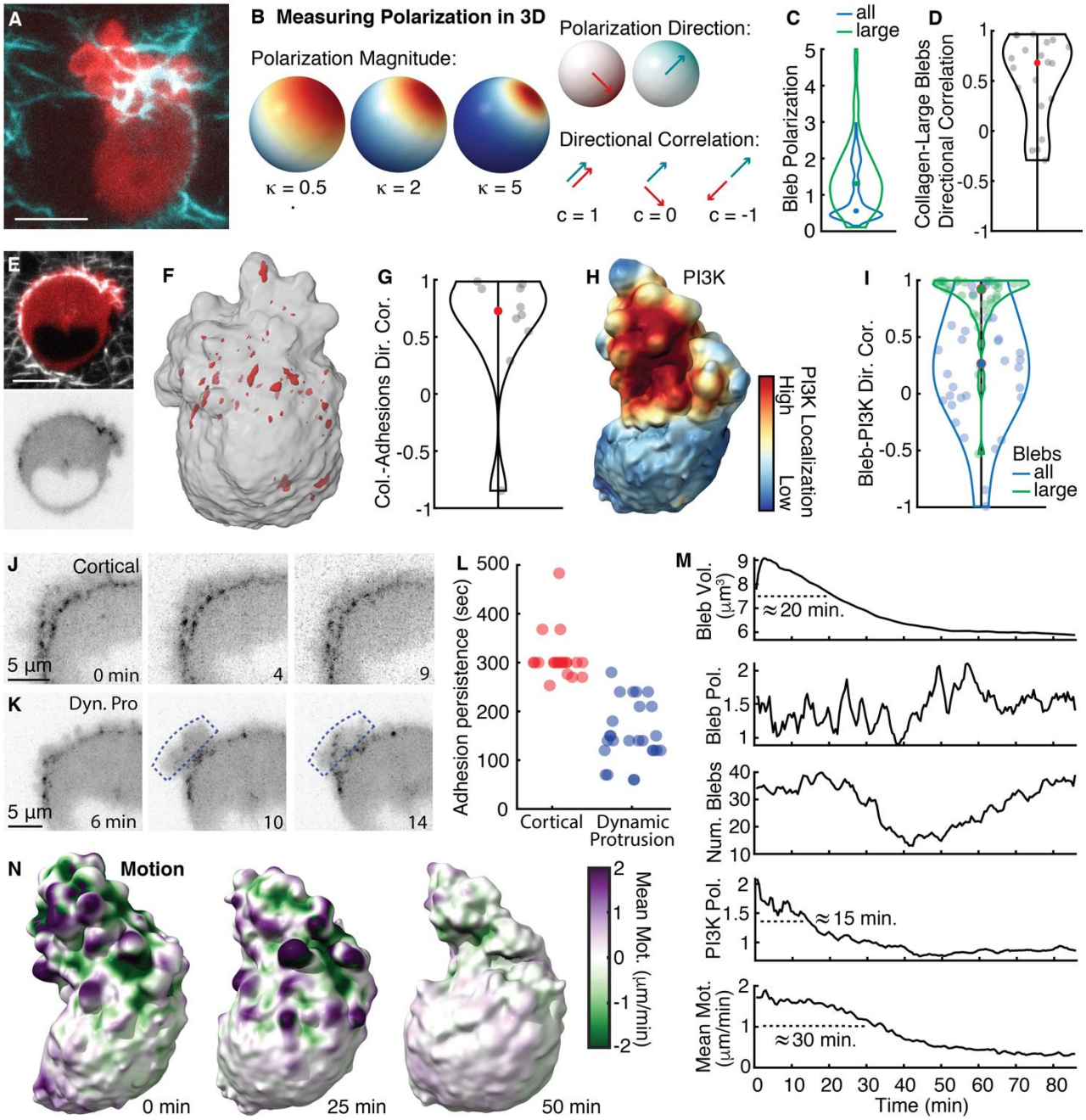

Figure 4. Worrying cells are polarized by adhesion signaling inside tunnels. (A) A single optical section of a light-sheet microscope image of an MV3 melanoma cell expressing GFP-AktPH (red) in 3D collagen (cyan). (B) Simulated species concentrations illustrating example polarization magnitudes and directional correlations. (C) Distributions of polarization magnitudes for all blebs (blue) and for the largest decile of blebs by volume (green). (n = 34 cells) (D) Directional correlation of collagen polarization near the cell surface with polarization of the largest decile of blebs. (E) Maximum intensity projections across 0.8 µm of a light-sheet microscope image of a melanoma cell expressing GFP-paxillin (red in top image, black in bottom image), in 3D collagen (white in top image). (F) A 3D surface rendering of a melanoma cell in 3D collagen with the cell surface shown transparent in gray and paxillin-marked adhesions in red. (G) The directional correlation of collagen polarization with adhesion polarization. (H)

A surface rendering of a light-sheet microscope image of a melanoma cell in collagen, colored by the localization of GFP-AktPH. (I) The directional correlation of bleb polarization with PI3K polarization for all blebs and for the largest decile of blebs by volume. (J) Time-lapse images of GFP-paxillin adhesions localized to the cortical region in a worrying cell. (K) Time-lapse images of GFP-paxillin adhesions within a dynamic protrusion, indicated by the dashed blue box. (L) Adhesion lifetimes for adhesions near the cell cortex (red) and within dynamic protrusions (blue) in three different cells for each condition. (M) Temporal response of an MV3 cell treated with FAK inhibitor 14. From top to bottom, shown are mean bleb volume, bleb polarization magnitude, number of blebs, PI3K polarization magnitude, and mean surface motion magnitude. Dashed lines indicate the approximate full-width half-maximum decay times of measures that are reduced by FAK inhibition. (N) Surface renderings colored by local surface motion of the cell shown analyzed in (N). Purple indicates protrusive regions, whereas green indicates retractive regions. Panel H shows PI3K localization on the same cell prior to treatment. Unless otherwise indicated, all scale bars show 10 μm.

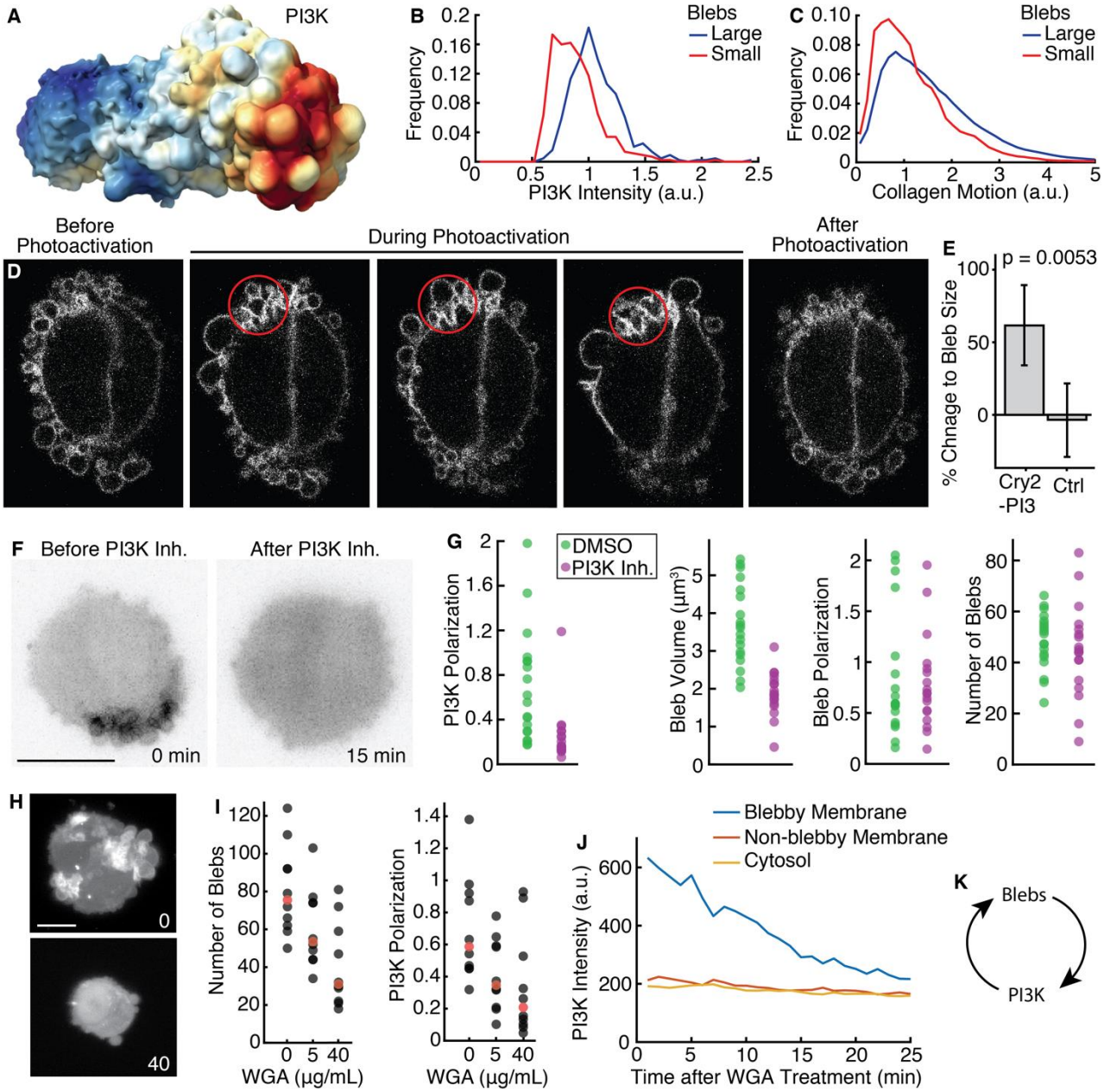

Figure 5. PI3K polarization creates large blebs. (A) A surface rendering of a light-sheet microscope image of a melanoma cell in collagen, colored by the localization of GFP-AktPH The corresponding colormap is shown in figure 4H. (B) Relative frequency distributions of GFP-AktPH near the cell surface separated according to PI3K products in large blebs (top decile by volume) or small blebs (bottom decile by volume) (n = 34 cells). (C) Frequency distributions of collagen motion near cell surfaces exhibiting large blebs (top decile by volume) or small blebs (bottom decile by volume) (n = 6 cells). (D) Spinning disk confocal microscope images showing a single optical slice of GFP-AktPH biosensor localization in an MV3 cell before, during and after photoactivation of PI3K in the area indicated by a red circle. (E) Change in bleb size due to photoactivation, calculated as mean maximum bleb area per bleb during activation divided by mean maximum bleb area per bleb in the same region before activation (p=0.0053, n=6 regions from 6 cells expressing mCherry-CRY2-iSH2 along with CIBN-CAAX and n=8 regions in 6 cells

not expressing cry2-mRuby2-PRL3) (F) Maximum intensity projections across 1.6 μm of a light-sheet microscope image of an MV3 cell expressing GFP-AktPH, before and after PI3K inhibition. (G) Effect of PI3Kα inhibitor IV compared to a DMSO control on bleb and PI3K properties in MV3 cells. PI3K polarization ($p = 0.001$) and bleb volume ($p = 9x10^{-8}$) show statistically significant differences across treatments, whereas bleb polarization ($p = 0.4$) and number of blebs ($p = 0.12$) do not. (H) Maximum intensity projection of light-sheet microscope images of representative melanoma cells treated with 0 μg/mL or 40 μg/mL wheat germ agglutinin (WGA). (I) The number of blebs and the PI3K polarization in individual cells as a function of WGA. In each category, the value of the median cell is colored red. (J) PI3K intensity as a function of time after WGA treatment in different regions of a cell. (K) Hypothetical positive feedback model for blebbing and PI3K signaling. All scale bars show 10 μm.

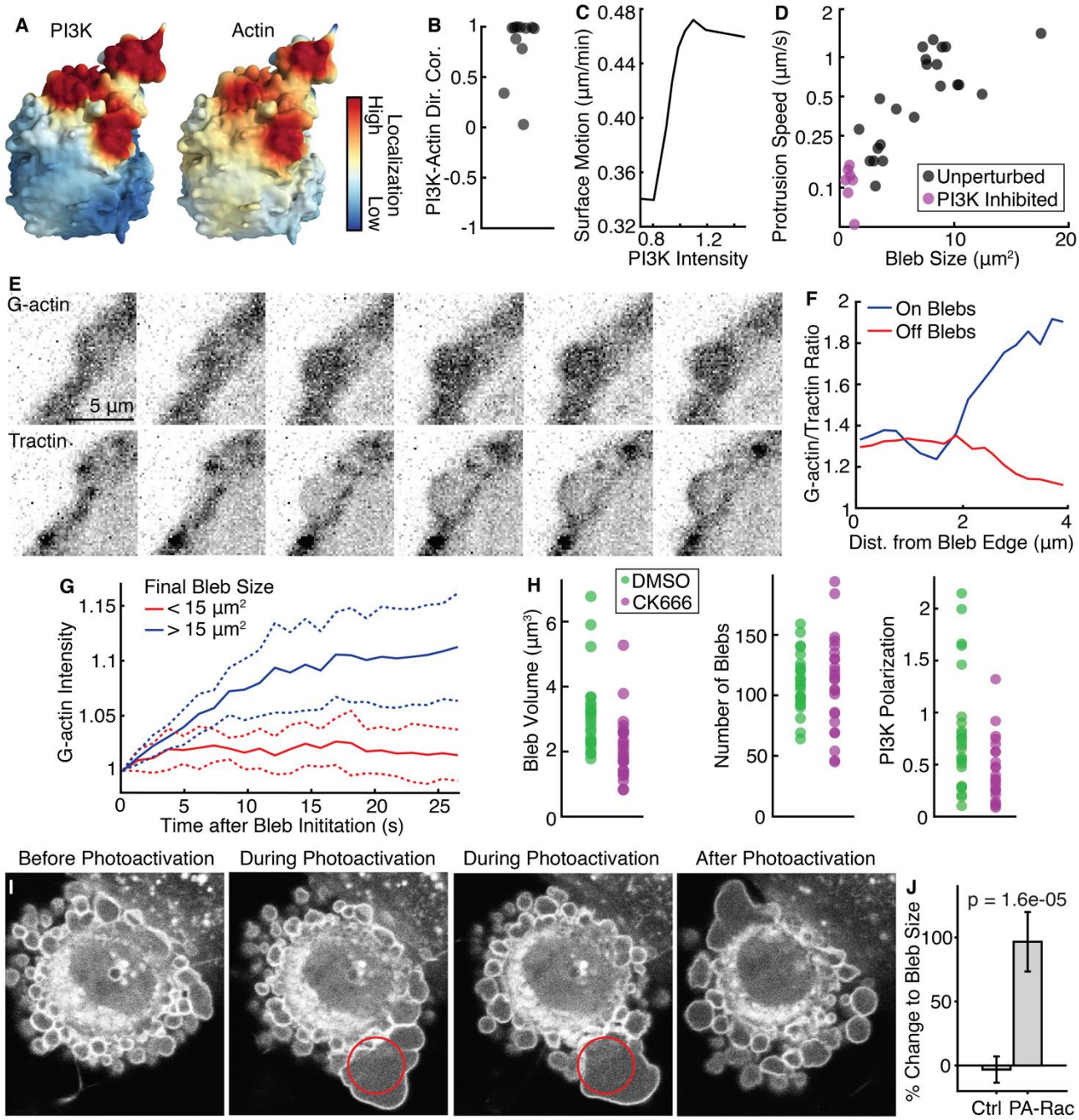

Figure 6. Rac1 creates large blebs through actin polymerization. (A) Surface renderings of 3D light-sheet microscopy images showing GFP-AktPH and HALO-actin intensity on the surface of an MV3 cell. (B) Directional correlation of PI3K and actin polarization in individual MV3 cells. (C) Local cell surface motion as a function of local PI3K intensity at the cell surface (n= 9 cells). (D) Protrusion speed of individual blebs as a function of final bleb size in either unperturbed or PI3K inhibited cells. (E) Time-lapse maximum intensity projections across 3.2 µm of HALO-actin and GFP-F-tractin in an MV3 cell . Volumes were acquired every 4.3 sec. (F) Actin/tractin ratio on and off blebs as a function of distance from the nearest bleb edge (n = 5 cells). (G) Actin intensity within large and small blebs as a function of time after bleb initiation. Dashed lines represent 95% confidence intervals (n= 12 blebs). (H) Effect of Arp2/3

inhibition via CK666 on PI3K and bleb properties, compared to DMSO control. PI3K polarization ($p = 0.004$) and bleb volume ($p = 0.001$) show statistically significant differences across samples, whereas the number of blebs do not ($p = 0.48$). (I) Spinning disk confocal microscope images showing a single optical slice of mCherry-PA-Rac1 in a MEF cell before, during and after photoactivation of PI3K in the area indicated by a red circle. (J) Change in bleb size due to photoactivation, calculated as mean maximum bleb area during activation divided by mean maximum bleb area in the same region before activation ($p=1.6 \times 10^{-5}$, n=6 regions expressing mCherry-PA-Rac1, n=11 regions in cells not expressing mCherry-PA-Rac1).

References

Abercrombie, M., Heaysman, J.E.M., Pegrum, S.M., 1970. The locomotion of fibroblasts in culture: III. Movements of particles on the dorsal surface of the leading lamella. Experimental Cell Research 62, 389–398. https://doi.org/10.1016/0014-4827(70)90570-7

Achrol, A.S., Rennert, R.C., Anders, C., Soffietti, R., Ahluwalia, M.S., Nayak, L., Peters, S., Arvold, N.D., Harsh, G.R., Steeg, P.S., Chang, S.D., 2019. Brain metastases. Nature Reviews Disease Primers 5, 1–26. https://doi.org/10.1038/s41572-018-0055-y

Aguet, F., Jacob, M., Unser, M., 2005. Three-dimensional feature detection using optimal steerable filters, in: 2005 International Conference on Image Processing (ICIP), Vols 1-5. Ieee, New York, pp. 2109–2112.

Andrew, N., Insall, R.H., 2007. Chemotaxis in shallow gradients is mediated independently of PtdIns 3-kinase by biased choices between random protrusions. Nat Cell Biol 9, 193–200. https://doi.org/10.1038/ncb1536

Appleton, S.E., Fadel, Z., Williams, J.S., Bezuhly, M., 2018. Vertical Growth Phase as a Prognostic Factor for Sentinel Lymph Node Positivity in Thin Melanomas: A Systematic Review and Meta-Analysis. Plast Reconstr Surg 141, 1529–1540. https://doi.org/10.1097/PRS.0000000000004395

Belin, B.J., Goins, L.M., Mullins, R.D., 2014. Comparative analysis of tools for live cell imaging of actin network architecture. Bioarchitecture 4, 189–202. https://doi.org/10.1080/19490992.2014.1047714

Bergert, M., Chandradoss, S.D., Desai, R.A., Paluch, E., 2012. Cell mechanics control rapid transitions between blebs and lamellipodia during migration. Proc. Natl. Acad. Sci. U.S.A. 109, 14434–14439. https://doi.org/10.1073/pnas.1207968109

Bisi, S., Disanza, A., Malinverno, C., Frittoli, E., Palamidessi, A., Scita, G., 2013. Membrane and actin dynamics interplay at lamellipodia leading edge. Current Opinion in Cell Biology, Cell adhesion and migration 25, 565–573. https://doi.org/10.1016/j.ceb.2013.04.001

Boekhorst, V. te, Jiang, L., Mählen, M., Meerlo, M., Dunkel, G., Durst, F.C., Yang, Y., Levine, H., Burgering, B.M.T., Friedl, P., 2020. Calpain-2 regulates hypoxia/HIF-induced amoeboid reprogramming and metastasis. bioRxiv 2020.01.06.892497. https://doi.org/10.1101/2020.01.06.892497

Bonnans, C., Chou, J., Werb, Z., 2014. Remodelling the extracellular matrix in development and disease. Nat. Rev. Mol. Cell Biol. 15, 786–801. https://doi.org/10.1038/nrm3904

Bordeleau, F., Mason, B.N., Lollis, E.M., Mazzola, M., Zanotelli, M.R., Somasegar, S., Califano, J.P., Montague, C., LaValley, D.J., Huynh, J., Mencia-Trinchant, N., Abril, Y.L.N., Hassane, D.C., Bonassar, L.J., Butcher, J.T., Weiss, R.S., Reinhart-King, C.A., 2017. Matrix stiffening promotes a tumor vasculature phenotype. PNAS 114, 492–497. https://doi.org/10.1073/pnas.1613855114

Buehler, M.J., 2006. Nature designs tough collagen: Explaining the nanostructure of collagen fibrils. PNAS 103, 12285–12290. https://doi.org/10.1073/pnas.0603216103

Burla, F., Dussi, S., Martinez-Torres, C., Tauber, J., Gucht, J. van der, Koenderink, G.H., 2020. Connectivity and plasticity determine collagen network fracture. PNAS 117, 8326–8334. https://doi.org/10.1073/pnas.1920062117

Calero-Cuenca, F.J., Janota, C.S., Gomes, E.R., 2018. Dealing with the nucleus during cell migration. Curr Opin Cell Biol 50, 35–41. https://doi.org/10.1016/j.ceb.2018.01.014

Charras, G.T., Coughlin, M., Mitchison, T.J., Mahadevan, L., 2008. Life and Times of a Cellular Bleb. Biophys J 94, 1836–1853. https://doi.org/10.1529/biophysj.107.113605

Charras, G.T., Hu, C.-K., Coughlin, M., Mitchison, T.J., 2006. Reassembly of contractile actin cortex in cell blebs. J Cell Biol 175, 477–490. https://doi.org/10.1083/jcb.200602085

Charras, G.T., Yarrow, J.C., Horton, M.A., Mahadevan, L., Mitchison, T.J., 2005. Non-equilibration of hydrostatic pressure in blebbing cells. Nature 435, 365–369. https://doi.org/10.1038/nature03550

Chen, B., Chou, H.-T., Brautigam, C.A., Xing, W., Yang, S., Henry, L., Doolittle, L.K., Walz, T., Rosen, M.K., 2017. Rac1 GTPase activates the WAVE regulatory complex through two distinct binding sites. eLife 6, e29795. https://doi.org/10.7554/eLife.29795

Chen, H.C., Guan, J.L., 1994. Association of focal adhesion kinase with its potential substrate phosphatidylinositol 3-kinase. Proceedings of the National Academy of Sciences of the United States of America 91, 10148–10152.

Choi, C.K., Vicente-Manzanares, M., Zareno, J., Whitmore, L.A., Mogilner, A., Horwitz, A.R., 2008. Actin and [alpha]-actinin orchestrate the assembly and maturation of nascent adhesions in a myosin II motor-independent manner. Nat Cell Biol 10, 1039–1050. https://doi.org/10.1038/ncb1763

Clark, E.A., Golub, T.R., Lander, E.S., Hynes, R.O., 2000. Genomic analysis of metastasis reveals an essential role for RhoC. Nature 406, 532–535. https://doi.org/10.1038/35020106

Cunningham, C.C., 1995. Actin polymerization and intracellular solvent flow in cell surface blebbing. J. Cell Biol. 129, 1589–1599.

Dean, K.M., Roudot, P., Reis, C.R., Welf, E.S., Mettlen, M., Fiolka, R., 2016. Diagonally Scanned Light-Sheet Microscopy for Fast Volumetric Imaging of Adherent Cells. Biophys. J. 110, 1456–1465. https://doi.org/10.1016/j.bpj.2016.01.029

Dean, K.M., Roudot, P., Welf, E.S., Danuser, G., Fiolka, R., 2015. Deconvolution-free Subcellular Imaging with Axially Swept Light Sheet Microscopy. Biophys. J. 108, 2807–2815. https://doi.org/10.1016/j.bpj.2015.05.013

Denais, C.M., Gilbert, R.M., Isermann, P., McGregor, A.L., te Lindert, M., Weigelin, B., Davidson, P.M., Friedl, P., Wolf, K., Lammerding, J., 2016. Nuclear envelope rupture and repair during cancer cell migration. Science 352, 353–358. https://doi.org/10.1126/science.aad7297

Devreotes, P., Horwitz, A.R., 2015. Signaling Networks that Regulate Cell Migration. Cold Spring Harb Perspect Biol 7, a005959. https://doi.org/10.1101/cshperspect.a005959

Diz-Muñoz, A., Krieg, M., Bergert, M., Ibarlucea-Benitez, I., Muller, D.J., Paluch, E., Heisenberg, C.-P., 2010. Control of directed cell migration in vivo by membrane-to-cortex attachment. PLoS Biol. 8, e1000544. https://doi.org/10.1371/journal.pbio.1000544

Driscoll, M.K., Welf, E.S., Jamieson, A.R., Dean, K.M., Isogai, T., Fiolka, R., Danuser, G., 2019. Robust and automated detection of subcellular morphological motifs in 3D microscopy images. Nat. Methods 16, 1037–1044. https://doi.org/10.1038/s41592-019-0539-z

Elliott, H., Fischer, R.S., Myers, K.A., Desai, R.A., Gao, L., Chen, C.S., Adelstein, R.S., Waterman, C.M., Danuser, G., 2015. Myosin II controls cellular branching morphogenesis and migration in three dimensions by minimizing cell-surface curvature. Nat. Cell Biol. 17, 137–147. https://doi.org/10.1038/ncb3092

Evans, E., Leung, A., 1984. Adhesivity and rigidity of erythrocyte membrane in relation to wheat germ agglutinin binding. J. Cell Biol. 98, 1201–1208.

Ferrari, R., Martin, G., Tagit, O., Guichard, A., Cambi, A., Voituriez, R., Vassilopoulos, S., Chavrier, P., 2019. MT1-MMP directs force-producing proteolytic contacts that drive tumor cell invasion. Nature Communications 10, 1–15. https://doi.org/10.1038/s41467-019-12930-y

Funamoto, S., Meili, R., Lee, S., Parry, L., Firtel, R.A., 2002. Spatial and Temporal Regulation of 3-Phosphoinositides by PI 3-Kinase and PTEN Mediates Chemotaxis. Cell 109, 611–623. https://doi.org/10.1016/S0092-8674(02)00755-9

Gadea, G., de Toledo, M., Anguille, C., Roux, P., 2007. Loss of p53 promotes RhoA–ROCK-dependent cell migration and invasion in 3D matrices. J Cell Biol 178, 23–30. https://doi.org/10.1083/jcb.200701120

Georgouli, M., Herraiz, C., Crosas-Molist, E., Fanshawe, B., Maiques, O., Perdrix, A., Pandya, P., Rodriguez-Hernandez, I., Ilieva, K.M., Cantelli, G., Karagiannis, P., Mele, S., Lam, H., Josephs, D.H., Matias-Guiu, X., Marti, R.M., Nestle, F.O., Orgaz, J.L., Malanchi, I., Fruhwirth, G.O., Karagiannis, S.N., Sanz-Moreno, V., 2019. Regional Activation of Myosin II in Cancer Cells Drives Tumor Progression via a Secretory Cross-Talk with the Immune Microenvironment. Cell 176, 757-774.e23. https://doi.org/10.1016/j.cell.2018.12.038

Goddard, T.D., Huang, C.C., Meng, E.C., Pettersen, E.F., Couch, G.S., Morris, J.H., Ferrin, T.E., 2018. UCSF ChimeraX: Meeting modern challenges in visualization and analysis. Protein Sci. 27, 14–25. https://doi.org/10.1002/pro.3235

González, G., Aguet, F., Fleuret, F., Unser, M., Fua, P., 2009. Steerable features for statistical 3D dendrite detection. Med Image Comput Comput Assist Interv 12, 625–632.

Goudarzi, M., Tarbashevich, K., Mildner, K., Begemann, I., Garcia, J., Paksa, A., Reichman-Fried, M., Mahabaleshwar, H., Blaser, H., Hartwig, J., Zeuschner, D., Galic, M., Bagnat, M., Betz, T., Raz, E., 2017. Bleb expansion in migrating cells depends on supply of membrane from cell surface invaginations. Dev Cell 43, 577-587.e5. https://doi.org/10.1016/j.devcel.2017.10.030

Guimarães, C.F., Gasperini, L., Marques, A.P., Reis, R.L., 2020. The stiffness of living tissues and its implications for tissue engineering. Nature Reviews Materials 5, 351–370. https://doi.org/10.1038/s41578-019-0169-1

Handorf, A.M., Zhou, Y., Halanski, M.A., Li, W.-J., 2015. Tissue Stiffness Dictates Development, Homeostasis, and Disease Progression. Organogenesis 11, 1–15. https://doi.org/10.1080/15476278.2015.1019687

Haugh, J.M., Codazzi, F., Teruel, M., Meyer, T., 2000. Spatial sensing in fibroblasts mediated by 3' phosphoinositides. J. Cell Biol 151, 1269–1280.

Idevall-Hagren, O., Dickson, E.J., Hille, B., Toomre, D.K., De Camilli, P., 2012. Optogenetic control of phosphoinositide metabolism. Proc. Natl. Acad. Sci. U.S.A. 109, E2316-2323. https://doi.org/10.1073/pnas.1211305109

Isogai, T., Dean, K.M., Roudot, P., Shao, Q., Cillay, J.D., Welf, E.S., Driscoll, M.K., Royer, S.P., Mittal, N., Chang, B.-J., Han, S.J., Fiolka, R., Danuser, G., 2019. Direct Arp2/3-vinculin binding is essential for cell spreading, but only on compliant substrates and in 3D. bioRxiv 756718. https://doi.org/10.1101/756718

Jacob, M., Unser, M., 2004. Design of steerable filters for feature detection using canny-like criteria. IEEE Trans Pattern Anal Mach Intell 26, 1007–1019. https://doi.org/10.1109/TPAMI.2004.44

Jannat, R.A., Dembo, M., Hammer, D.A., 2011. Traction Forces of Neutrophils Migrating on Compliant Substrates. Biophys J 101, 575–584. https://doi.org/10.1016/j.bpj.2011.05.040

Johnson, H.E., King, S.J., Asokan, S.B., Rotty, J.D., Bear, J.E., Haugh, J.M., 2015. F-actin bundles direct the initiation and orientation of lamellipodia through adhesion-based signaling. J. Cell Biol. 208, 443–455. https://doi.org/10.1083/jcb.201406102

Kardash, E., Reichman-Fried, M., Maître, J.-L., Boldajipour, B., Papusheva, E., Messerschmidt, E.-M., Heisenberg, C.-P., Raz, E., 2010. A role for Rho GTPases and cell-cell adhesion in single-cell motility in vivo. Nat. Cell Biol. 12, 47–53; sup pp 1-11. https://doi.org/10.1038/ncb2003

Kerr, M.C., Teasdale, R.D., 2009. Defining macropinocytosis. Traffic 10, 364–371. https://doi.org/10.1111/j.1600-0854.2009.00878.x

Kessenbrock, K., Plaks, V., Werb, Z., 2010. Matrix Metalloproteinases: Regulators of the Tumor Microenvironment. Cell 141, 52–67. https://doi.org/10.1016/j.cell.2010.03.015

Lammerding, J., 2011. Mechanics of the Nucleus, in: Comprehensive Physiology. American Cancer Society, pp. 783–807. https://doi.org/10.1002/cphy.c100038

Lauffenburger, D.A., Horwitz, A.F., 1996. Cell migration: a physically integrated molecular process. Cell 84, 359–369. https://doi.org/10.1016/s0092-8674(00)81280-5

Laukaitis, C.M., Webb, D.J., Donais, K., Horwitz, A.F., 2001. Differential dynamics of alpha 5 integrin, paxillin, and alpha-actinin during formation and disassembly of adhesions in migrating cells. J Cell Biol 153, 1427–1440. https://doi.org/10.1083/jcb.153.7.1427

Liu, Y.-J., Le Berre, M., Lautenschlaeger, F., Maiuri, P., Callan-Jones, A., Heuzé, M., Takaki, T., Voituriez, R., Piel, M., 2015. Confinement and Low Adhesion Induce Fast Amoeboid Migration of Slow Mesenchymal Cells. Cell 160, 659–672. https://doi.org/10.1016/j.cell.2015.01.007

Lomakin, A.J., Cattin, C.J., Cuvelier, D., Alraies, Z., Molina, M., Nader, G.P.F., Srivastava, N., Sáez, P.J., Garcia-Arcos, J.M., Zhitnyak, I.Y., Bhargava, A., Driscoll, M.K., Welf, E.S., Fiolka, R., Petrie, R.J., De Silva, N.S., González-Granado, J.M., Manel, N., Lennon-Duménil, A.M., Müller, D.J., Piel, M., 2020. The nucleus acts as a ruler tailoring cell responses to spatial constraints. Science 370. https://doi.org/10.1126/science.aba2894

Ma, M., Baumgartner, M., 2013. Filopodia and Membrane Blebs Drive Efficient Matrix Invasion of Macrophages Transformed by the Intracellular Parasite Theileria annulata. PLoS ONE 8, e75577. https://doi.org/10.1371/journal.pone.0075577

Maaser, K., Wolf, K., Klein, C.E., Niggemann, B., Zänker, K.S., Bröcker, E.B., Friedl, P., 1999. Functional hierarchy of simultaneously expressed adhesion receptors: integrin alpha2beta1 but not CD44 mediates MV3 melanoma cell migration and matrix reorganization within three-dimensional hyaluronan-containing collagen matrices. Mol Biol Cell 10, 3067–3079. https://doi.org/10.1091/mbc.10.10.3067

Madsen, C.D., Hooper, S., Tozluoglu, M., Bruckbauer, A., Fletcher, G., Erler, J.T., Bates, P.A., Thompson, B., Sahai, E., 2015. STRIPAK components determine mode of cancer cell migration and metastasis. Nat. Cell Biol. 17, 68–80. https://doi.org/10.1038/ncb3083

Manandhar, S., Bouthemy, P., Welf, E., Danuser, G., Roudot, P., Kervrann, C., 2020. 3D flow field estimation and assessment for live cell fluorescence microscopy. Bioinformatics 36, 1317–1325. https://doi.org/10.1093/bioinformatics/btz780

Masereel, B., Pochet, L., Laeckmann, D., 2003. An overview of inhibitors of Na+/H+ exchanger. European Journal of Medicinal Chemistry 38, 547–554. https://doi.org/10.1016/S0223-5234(03)00100-4

Nolen, B.J., Tomasevic, N., Russell, A., Pierce, D.W., Jia, Z., McCormick, C.D., Hartman, J., Sakowicz, R., Pollard, T.D., 2009. Characterization of two classes of small molecule inhibitors of Arp2/3 complex. Nature 460, 1031–1034. https://doi.org/10.1038/nature08231

Orgaz, J.L., Pandya, P., Dalmeida, R., Karagiannis, P., Sanchez-Laorden, B., Viros, A., Albrengues, J., Nestle, F.O., Ridley, A.J., Gaggioli, C., Marais, R., Karagiannis, S.N., Sanz-Moreno, V., 2014. Diverse matrix metalloproteinase functions regulate cancer amoeboid migration. Nat Commun 5, 4255. https://doi.org/10.1038/ncomms5255

Paluch, E.K., Raz, E., 2013. The role and regulation of blebs in cell migration. Current Opinion in Cell Biology 25, 582–590. https://doi.org/10.1016/j.ceb.2013.05.005

Petrie, R.J., Gavara, N., Chadwick, R.S., Yamada, K.M., 2012. Nonpolarized signaling reveals two distinct modes of 3D cell migration. J. Cell Biol. 197, 439–455. https://doi.org/10.1083/jcb.201201124

Petrie, R.J., Koo, H., Yamada, K.M., 2014. Generation of compartmentalized pressure by a nuclear piston governs cell motility in a 3D matrix. Science 345, 1062–1065. https://doi.org/10.1126/science.1256965

Petrie, R.J., Yamada, K.M., 2016. Multiple mechanisms of 3D migration: the origins of plasticity. Curr Opin Cell Biol 42, 7–12. https://doi.org/10.1016/j.ceb.2016.03.025

Pinner, S., Sahai, E., 2008. PDK1 regulates cancer cell motility by antagonising inhibition of ROCK1 by RhoE. Nat. Cell Biol. 10, 127–137. https://doi.org/10.1038/ncb1675

Provenzano, P.P., Inman, D.R., Eliceiri, K.W., Keely, P.J., 2009. Matrix density-induced mechanoregulation of breast cell phenotype, signaling and gene expression through a FAK–ERK linkage. Oncogene 28, 4326–4343. https://doi.org/10.1038/onc.2009.299

Quintana, E., Piskounova, E., Shackleton, M., Weinberg, D., Eskiocak, U., Fullen, D.R., Johnson, T.M., Morrison, S.J., 2012. Human Melanoma Metastasis in NSG Mice Correlates with Clinical Outcome in Patients. Sci Transl Med 4, 159ra149-159ra149. https://doi.org/10.1126/scitranslmed.3004599

Rao, S.S., Bentil, S., DeJesus, J., Larison, J., Hissong, A., Dupaix, R., Sarkar, A., Winter, J.O., 2012. Inherent Interfacial Mechanical Gradients in 3D Hydrogels Influence Tumor Cell Behaviors. PLoS ONE 7, e35852. https://doi.org/10.1371/journal.pone.0035852

Recouvreux, M.V., Commisso, C., 2017. Macropinocytosis: A Metabolic Adaptation to Nutrient Stress in Cancer. Front Endocrinol (Lausanne) 8, 261. https://doi.org/10.3389/fendo.2017.00261

Renkawitz, J., Kopf, A., Stopp, J., de Vries, I., Driscoll, M.K., Merrin, J., Hauschild, R., Welf, E.S., Danuser, G., Fiolka, R., Sixt, M., 2019. Nuclear positioning facilitates amoeboid migration along the path of least resistance. Nature 568, 546–550. https://doi.org/10.1038/s41586-019-1087-5

Rodriguez-Hernandez, I., Maiques, O., Kohlhammer, L., Cantelli, G., Perdrix-Rosell, A., Monger, J., Fanshawe, B., Bridgeman, V.L., Karagiannis, S.N., Penin, R.M., Marcolval, J., Marti, R.M., Matias-Guiu, X., Fruhwirth, G.O., Orgaz, J.L., Malanchi, I., Sanz-Moreno, V., 2020. WNT11-FZD7-DAAM1 signalling supports tumour initiating abilities and melanoma amoeboid invasion. Nature Communications 11, 5315. https://doi.org/10.1038/s41467-020-18951-2

Roh-Johnson, M., Shah, A.N., Stonick, J.A., Poudel, K.R., Kargl, J., Yang, G.H., di Martino, J., Hernandez, R.E., Gast, C.E., Zarour, L.R., Antoku, S., Houghton, A.M., Bravo-Cordero, J.J., Wong, M.H., Condeelis, J., Moens, C.B., 2017. Macrophage-Dependent Cytoplasmic Transfer during Melanoma Invasion In Vivo. Dev Cell 43, 549-562.e6. https://doi.org/10.1016/j.devcel.2017.11.003

Sadok, A., McCarthy, A., Caldwell, J., Collins, I., Garrett, M.D., Yeo, M., Hooper, S., Sahai, E., Kuemper, S., Mardakheh, F.K., Marshall, C.J., n.d. Rho Kinase Inhibitors Block Melanoma Cell Migration and Inhibit Metastasis [WWW Document]. URL http://cancerres.aacrjournals.org (accessed 12.20.15).

Sahai, E., Marshall, C.J., 2003. Differing modes of tumour cell invasion have distinct requirements for Rho/ROCK signalling and extracellular proteolysis. Nat. Cell Biol. 5, 711–719. https://doi.org/10.1038/ncb1019

Sanz-Moreno, V., Gadea, G., Ahn, J., Paterson, H., Marra, P., Pinner, S., Sahai, E., Marshall, C.J., 2008. Rac activation and inactivation control plasticity of tumor cell movement. Cell 135, 510–523. https://doi.org/10.1016/j.cell.2008.09.043

Sanz-Moreno, V., Gaggioli, C., Yeo, M., Albrengues, J., Wallberg, F., Viros, A., Hooper, S., Mitter, R., Féral, C.C., Cook, M., Larkin, J., Marais, R., Meneguzzi, G., Sahai, E., Marshall, C.J., 2011. ROCK and JAK1 signaling cooperate to control actomyosin contractility in tumor cells and stroma. Cancer Cell 20, 229–245. https://doi.org/10.1016/j.ccr.2011.06.018

Schell, M.J., Erneux, C., Irvine, R.F., 2001. Inositol 1,4,5-trisphosphate 3-kinase A associates with F-actin and dendritic spines via its N terminus. J. Biol. Chem. 276, 37537–37546. https://doi.org/10.1074/jbc.M104101200

Sherman, V.R., Yang, W., Meyers, M.A., 2015. The materials science of collagen. Journal of the Mechanical Behavior of Biomedical Materials, SI:Collagen mechanics 52, 22–50. https://doi.org/10.1016/j.jmbbm.2015.05.023

Stroka, K.M., Jiang, H., Chen, S.-H., Tong, Z., Wirtz, D., Sun, S.X., Konstantopoulos, K., 2014. Water Permeation Drives Tumor Cell Migration in Confined Microenvironments. Cell 157, 611–623. https://doi.org/10.1016/j.cell.2014.02.052

Tozluoğlu, M., Tournier, A.L., Jenkins, R.P., Hooper, S., Bates, P.A., Sahai, E., 2013. Matrix geometry determines optimal cancer cell migration strategy and modulates response to interventions. Nat. Cell Biol. 15, 751–762. https://doi.org/10.1038/ncb2775

Venturini, V., Pezzano, F., Castro, F.C., Häkkinen, H.-M., Jiménez-Delgado, S., Colomer-Rosell, M., Marro, M., Tolosa-Ramon, Q., Paz-López, S., Valverde, M.A., Weghuber, J., Loza-Alvarez, P., Krieg, M., Wieser, S., Ruprecht, V., 2020. The nucleus measures shape changes for cellular proprioception to control dynamic cell behavior. Science 370. https://doi.org/10.1126/science.aba2644

Wang, H., Abhilash, A.S., Chen, C., Wells, R., Shenoy, V., 2014. Long-Range Force Transmission in Fibrous Matrices Enabled by Tension-Driven Alignment of Fibers. Biophysical Journal 107, 2592–2603. https://doi.org/10.1016/j.bpj.2014.09.044

Welch, H.C.E., Coadwell, W.J., Stephens, L.R., Hawkins, P.T., 2003. Phosphoinositide 3-kinase-dependent activation of Rac. FEBS Letters 546, 93–97. https://doi.org/10.1016/S0014-5793(03)00454-X

Welf, E.S., Ahmed, S., Johnson, H.E., Melvin, A.T., Haugh, J.M., 2012. Migrating fibroblasts reorient directionality by a metastable, PI3K-dependent mechanism. J. Cell Biol. 197, 105–114. https://doi.org/10.1083/jcb.201108152

Welf, E.S., Driscoll, M.K., Dean, K.M., Schäfer, C., Chu, J., Davidson, M.W., Lin, M.Z., Danuser, G., Fiolka, R., 2016. Quantitative Multiscale Cell Imaging in Controlled 3D Microenvironments. Dev. Cell 36, 462–475. https://doi.org/10.1016/j.devcel.2016.01.022

Welf, E.S., Miles, C.E., Huh, J., Driscoll, M.K., Isogai, T., Noh, J., Weems, A.D., Chi, J., Pohlkamp, T., Dean, K., Fiolka, R., Mogilner, A., Danuser, G., 2019. A unified role for membrane-cortex detachment during cell protrusion initiation. bioRxiv 696211. https://doi.org/10.1101/696211

Wolf, K., Mazo, I., Leung, H., Engelke, K., von Andrian, U.H., Deryugina, E.I., Strongin, A.Y., Bröcker, E.-B., Friedl, P., 2003. Compensation mechanism in tumor cell migration: mesenchymal-amoeboid transition after blocking of pericellular proteolysis. J. Cell Biol. 160, 267–277. https://doi.org/10.1083/jcb.200209006

Wolf, K., Te Lindert, M., Krause, M., Alexander, S., Te Riet, J., Willis, A.L., Hoffman, R.M., Figdor, C.G., Weiss, S.J., Friedl, P., 2013. Physical limits of cell migration: Control by ECM space and nuclear deformation and tuning by proteolysis and traction force. J. Cell Biol. 201, 1069–1084. https://doi.org/10.1083/jcb.201210152

Wolf, K., Wu, Y.I., Liu, Y., Geiger, J., Tam, E., Overall, C., Stack, M.S., Friedl, P., 2007. Multi-step pericellular proteolysis controls the transition from individual to collective cancer cell invasion. Nature Cell Biology 9, 893–904. https://doi.org/10.1038/ncb1616

Wu, Y.I., Frey, D., Lungu, O.I., Jaehrig, A., Schlichting, I., Kuhlman, B., Hahn, K.M., 2009. A genetically encoded photoactivatable Rac controls the motility of living cells. Nature 461, 104–108. https://doi.org/10.1038/nature08241

Wyckoff, J.B., Pinner, S.E., Gschmeissner, S., Condeelis, J.S., Sahai, E., 2006. ROCK- and myosin-dependent matrix deformation enables protease-independent tumor-cell invasion in vivo. Curr. Biol. 16, 1515–1523. https://doi.org/10.1016/j.cub.2006.05.065

Yamada, K.M., Sixt, M., 2019. Mechanisms of 3D cell migration. Nature Reviews Molecular Cell Biology 20, 738–752. https://doi.org/10.1038/s41580-019-0172-9

Yamazaki, S., Su, Y., Maruyama, A., Makinoshima, H., Suzuki, J., Tsuboi, M., Goto, K., Ochiai, A., Ishii, G., 2020. Uptake of collagen type I via macropinocytosis cause mTOR activation and anti-cancer drug resistance. Biochemical and Biophysical Research Communications 526, 191–198. https://doi.org/10.1016/j.bbrc.2020.03.067

Zaritsky, A., Jamieson, A.R., Welf, E.S., Nevarez, A., Cillay, J., Eskiocak, U., Cantarel, B.L., Danuser, G., 2020. Interpretable deep learning of label-free live cell images uncovers functional hallmarks of highly-metastatic melanoma. bioRxiv 2020.05.15.096628. https://doi.org/10.1101/2020.05.15.096628

Zhan, H., Bhattacharya, S., Cai, H., Iglesias, P.A., Huang, C.-H., Devreotes, P.N., 2020. An Excitable Ras/PI3K/ERK Signaling Network Controls Migration and Oncogenic Transformation in Epithelial Cells. Dev Cell 54, 608-623.e5. https://doi.org/10.1016/j.devcel.2020.08.001